THE GEOLOGICAL SOCIETY OF AMERICA®

Mud cohesion governs unvegetated meander migration rates and deposit architecture

Madison M. Douglas[1,2,†], Kimberly Litwin Miller[1], and Michael P. Lamb[1]
[1]*Division of Geological and Planetary Sciences, California Institute of Technology, Pasadena, California 91125, USA*
[2]*Department of Earth, Atmospheric, and Planetary Science, Massachusetts Institute of Technology, Cambridge, Massachusetts 02139, USA*

ABSTRACT

Vegetation is thought to be a main source of riverbank cohesion, enabling meandering and a deposit architecture characterized by sandy channel belts isolated in mudstone. However, early Earth and Mars had meandering rivers without vegetation, implying that other sources of bank strength can allow meandering with potentially different deposit characteristics. Here we studied the Amargosa River in Death Valley, California, USA, as a modern analog of meandering rivers without vegetation. We monitored flow and erosion at two bends and used radiocarbon dating of strandlines to quantify flood frequency. We also sampled cutbank mud and constrained an erosion theory using flume experiments. Cutbank erosion occurred for floods with >2 yr recurrence intervals, and 18 cm occurred for an ~6 yr reoccurrence, bankfull event. Mud set the rate of meander migration: salt crusts rapidly and completely dissolved during floods, vegetation was absent, and mud entrainment theory matched observed erosion rates. Flood-frequency analysis showed that most bank erosion occurs at flows below bankfull, challenging the threshold channel hypothesis. We used meander migration rates to constrain the time scale of channel-belt formation and compared it to the time scale of avulsion. These calculations, combined with floodplain facies mapping and core sedimentology, indicated a likely deposit architecture of sandy point bar accretion sets intermixed with muddy overbank facies. This deposit architecture is characteristic of vegetated meandering rivers, but due to muddy banks, occurred for the Amargosa River in the absence of plants.

INTRODUCTION

Many rivers can be classified as meandering or braided (Fig. 1; Leopold and Wolman, 1957; Parker, 1976), and the factors that determine these fundamental planform geometries are debated. Meandering is thought to require a bank-strengthening agent that slows cutbank erosion and allows point-bar accretion to keep pace, maintaining a relatively narrow channel width (e.g., Eke et al., 2014). In the absence of a bank strengthening agent, cutbank erosion can be rapid, forcing river widening and eventually braiding (Parker et al., 2011; Métivier et al., 2017). Riverbank strength sufficient to permit river meandering is often attributed to vegetation or vegetated slump blocks (Millar, 2000; Corenblit and Steiger, 2009; Parker et al., 2011). Vegetation may strengthen the bank material either directly, through root binding (Abernethy and Rutherfurd, 2001; Pollen-Bankhead and Simon, 2009), or indirectly, through promoting mud deposition by baffling the flow (Kleinhans et al., 2018) and organic material-mediated flocculation (Zeichner et al., 2021; Nghiem et al., 2022), or by preventing wind erosion of fluvial deposits (Sweeney et al., 2019). The rock record also records a shift in fluvial deposit architecture with the evolution of land plants from predominantly amalgamated sandy channel-belt deposits to predominantly muddy overbank facies with isolated sandstone bodies (McMahon and Davies, 2018). This fundamental shift in the nature of fluvial deposit architecture likewise has been interpreted to reflect a change in dominant river planform geometry from sandy braid plains to meandering rivers with muddy floodplains tied to the colonization of floodplains with plants (Fig. 1; Long, 1978; Sweet, 1988; McMahon and Davies, 2018), though this interpretation is debated (Ganti et al., 2019; Ielpi et al., 2022).

While vegetation may promote meandering for many of the world's rivers, there exist modern examples of meandering rivers in drylands, where vegetation is sparse or absent (Matsubara et al., 2015; Li et al., 2015; Ielpi and Lapôtre, 2019). In addition, there is evidence for meandering rivers in the ancient rock record dating to before land plants (Ielpi and Rainbird, 2015; Santos and Owen, 2016; Ganti et al., 2019; Valenza et al., 2023), as well as evidence of point bar growth and cutoff on ancient Mars (Malin and Edgett, 2003; Burr et al., 2009). For these rivers, a source of riverbank strength other than vegetation would seem to be required (Matsubara et al., 2015; Lapôtre et al., 2019). Potential sources of bank strength include cohesive mud and salt crusts (Millar and Quick, 1998; Matsubara et al., 2015; Dong et al., 2019). Mud has a high critical shear stress for entrainment and can provide strength through its material cohesion (Hanson and Simon, 2001; Julian and Torres, 2006; Dunne and Jerolmack, 2020). Salt crusts might provide strength through chemical cementation within the bank (Ritter et al., 2022). While mud and salt crusts have become favored hypotheses for meandering without plants (Millar, 2005; Matsubara et al., 2015; Lapôtre et al., 2019), the effectiveness of each mechanism is unknown.

Moreover, despite the existence of unvegetated meandering rivers with similar morphologic features and width-to-depth ratios as vegetated meanders (Ielpi, 2019; Santos et al., 2019), it is unclear whether these rivers have different properties from their vegetated counterparts. For example, the leading theory for river channel geometry, which is used in paleo-hydraulic reconstructions of unvegetated rivers on Earth and Mars (e.g., DiBiase et al., 2013; Lapôtre et al., 2019; Ganti et al., 2019; Hayden et al., 2019), posits that channels evolve to a shape where the bank material is at the threshold of entrainment when the river is at bankfull (Parker, 1978). This hypothesis describes gravel-bedded rivers well, where channel geometry is set by the threshold to move gravel on the banks while maintaining a mobile bed (Phillips and Jerolmack, 2016; Métivier et al., 2017). However, vegetated sand-bedded rivers require substantial

Madison M. Douglas https://orcid.org/0000-0002-0762-4719
[†]mmdouglas@berkeley.edu

GSA Bulletin; January/February 2025; v. 137; no. 1/2; p. 522–540; https://doi.org/10.1130/B37315.1.
Published online 19 July 2024

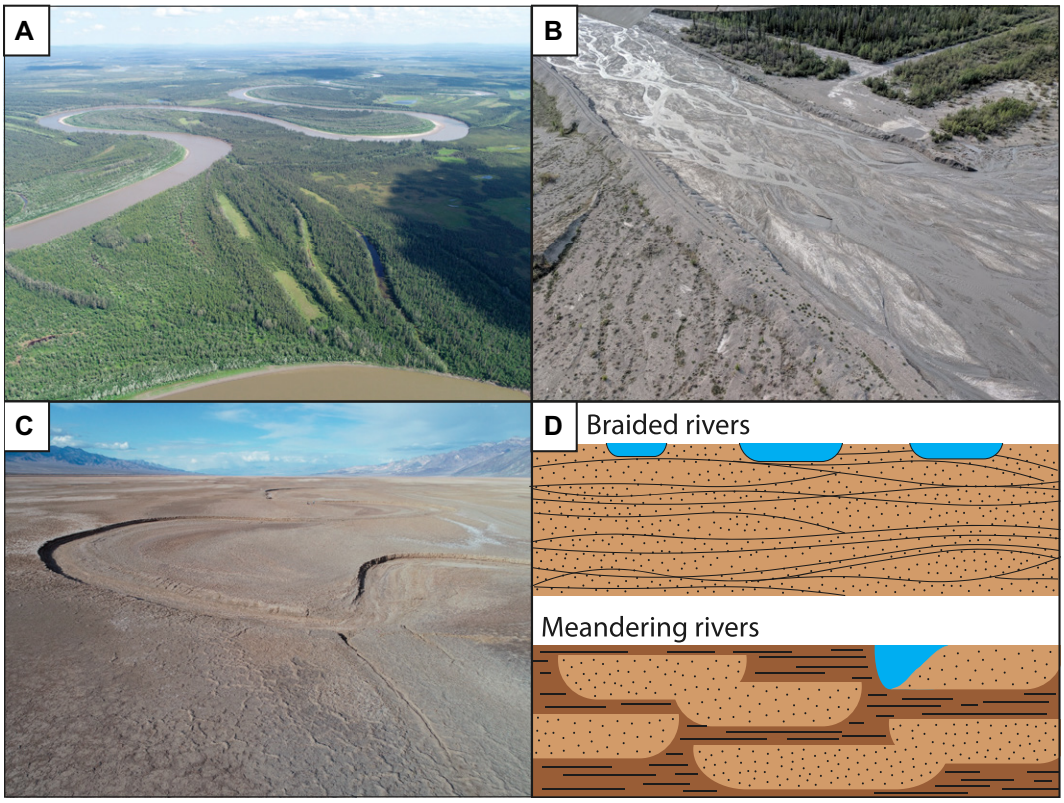

Figure 1. Contrasting river planform morphologies and stratigraphic architectures. (A) A meandering reach of the Koyukuk River near Huslia, Alaska, USA. The aerial image was taken in summer 2018, and the river is ~300 m wide in the image. (B) The braided Kaskawulsh River, Yukon Territory, Canada. Photo taken from small aircraft by Madison Douglas. (C) Aerial image of an unvegetated, meandering reach of the Amargosa River, Death Valley, California, USA. The river cutbank is ~1 m high. (D) Cartoon showing one hypothesis for braided and meandering river stratigraphic architecture. Coarser sandy deposits are shown in speckled light brown, finer muddy deposits are dark brown with short lines, and active channels are shown at bankfull stage in light blue.

bank strength of ~10 Pa to conform to threshold channel theory (Dunne and Jerolmack, 2020), which is far greater than the shear stress required to entrain sand. In the absence of vegetation as a bank strengthening agent, do rivers still follow threshold channel theory? And if so, would the value for the threshold bank stress be substantially different for a river where the bank strength is controlled by mud or salt rather than vegetation?

Another major question pertains to the rate at which unvegetated rivers meander and how this affects deposit architecture. A recent study used remote sensing to show that lateral migration rates of selected dryland rivers are ten times faster than migration rates of selected vegetated rivers that have similar channel width, despite the arid climate of the dryland rivers (Ielpi and Lapôtre, 2020). These measurements averaged channel migration over many flood events making it difficult to directly test bank erosion theory and to separate the relative roles of bank strength from flood frequency in driving differences in meander rates across climatic zones. Nonetheless, if these observations are generally true, they reinforce the controlling role that vegetation might have on slowing meander lateral migration rates, which in turn should affect deposit architecture (e.g., Hasson et al., 2023). In particular, rivers that meander across their floodplain rapidly compared to the time scale of channel avulsion tend to build deposits that consist of amalgamated sandstone with little preserved mudstone (Jerolmack and Mohrig, 2007; Hartley et al., 2015). That is, the hypothesized rapid lateral migration rate of unvegetated rivers could potentially explain the change to a mudrock-dominated fluvial architecture that occurred with the proliferation of land plants in the Silurian without necessitating a fundamental change in river form from braided to meandering (Valenza et al., 2023).

To better understand river dynamics and deposit characteristics for unvegetated meandering rivers, we conducted a multi-year field study on a meandering reach of the Amargosa River on the floor of Death Valley, California, USA (Fig. 2). We monitored channel hydraulics and used radiocarbon dating of historic flood deposits to develop a relation for flood frequency and magnitude. In addition, we calibrated a bank erosion model using direct observations of cutbank erosion and a novel experimental setup where we eroded samples of bank material under controlled conditions. Together these data were used to understand whether salt crusts or mud were the limiting agent for bank erosion in our reach. Because our measurements were made on the flood time scale rather than averaged over years or decades as in previous work, we were able to directly link bank erosion rates to mud entrainment theory and parse the relative roles of flood frequency and flood magnitude on net bank erosion. We used our measurements to assess whether unvegetated ephemeral channels follow threshold channel theory, which is commonly employed but largely untested when reconstructing paleo-hydraulics of ancient unvegetated rivers on Earth and Mars. Finally, to understand deposit architecture, we used migration rates along with valley aggradation rates from dated cores to constrain the time scale of channel migration across the floodplain relative to the time scale of channel avulsion. These rates, combined with floodplain facies mapping and core sedimentology, were used to infer the likely deposit architecture of the subsurface.

STUDY SITE

We studied the lower reaches of the Amargosa river as it traverses Death Valley National Park to Badwater Basin, the lowest point in North America at 86 m below sea level that has the highest recorded air temperature of 57 °C (Fig. 2). In this area, the Amargosa River contains multiple distributary channels, some with meandering reaches, and little to no vegetation (Baldridge et al., 2004; Ielpi, 2019). By analyzing aerial imagery (4–6 m resolution) from 1977 to 2007, the Amargosa meanders were previously reported to actively migrate at decadal rates up to 1.5 m/yr (Ielpi, 2019), higher than

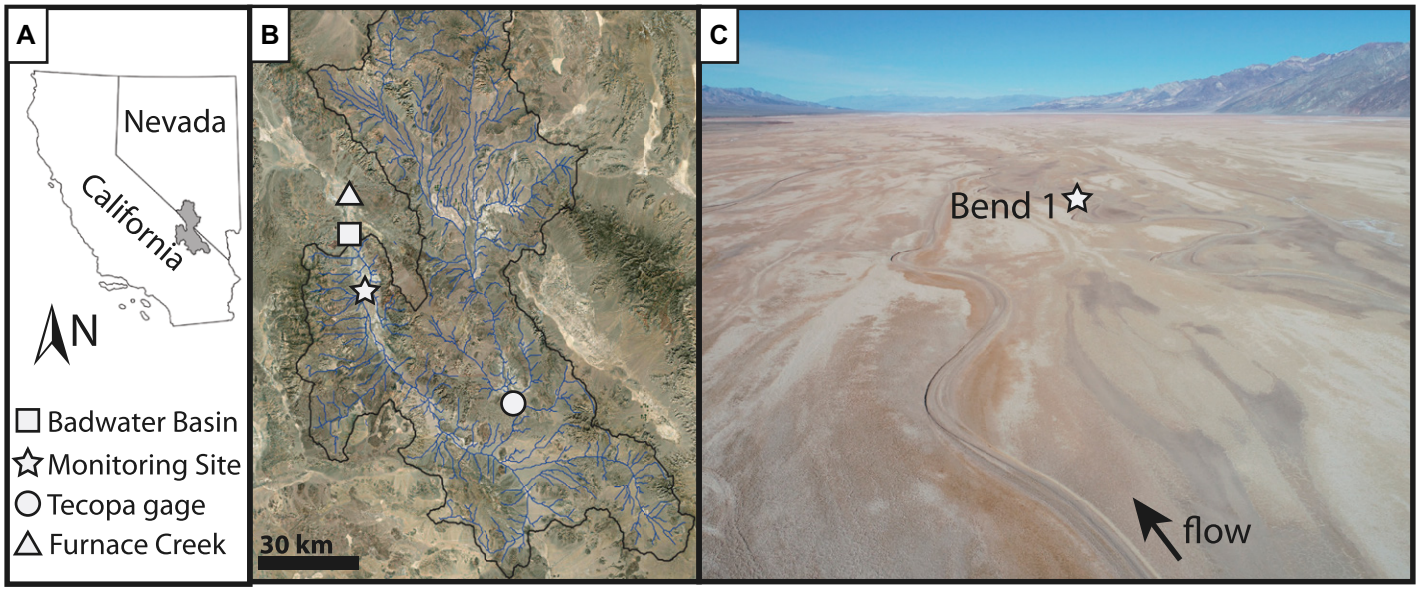

Figure 2. Context of Amargosa River and study bends. (A) The Amargosa watershed is shaded gray on the state outlines. (B) The Amargosa runs from the Amargosa Valley, Nevada, USA, to Badwater Basin in California (square), past a U.S. Geological Survey stream gage in Tecopa, California, USA (circle). The area of the catchment at our monitoring site (star) receives water from upstream as well as alluvial fans coming off the Black (east) and Panamint (west) ranges. (C) Aerial image taken looking north toward Badwater Basin overlooking the Bend 1 monitoring site (image taken January 2021).

width-normalized migration rates for most vegetated meandering rivers (Ielpi and Lapôtre, 2020; Langhorst and Pavelsky, 2023). This result is surprising given the strongly ephemeral nature of these desert rivers.

The Amargosa River originates in the Amargosa Valley, Nevada, USA, and flows south before turning and flowing north to Badwater Basin, California (Fig. 2). Its watershed is largely protected from anthropogenic alteration due to land conservation efforts. The study reach is bounded on the west by Panamint Range and east by the Black Mountains, which supply water and sediment to the Amargosa via alluvial fans. The Amargosa's bedload contains gravel when it enters Death Valley, but the sediment supply to our study reach consists of fine sand and smaller material (Ielpi, 2019). Death Valley is subsiding along faults striking north to south along the eastern and western edges of the valley. The eastern fault has a slip rate greater than the western bounding fault, causing tilting of ~0.016°/k.y. at present (Hooke, 1972).

During the last glacial period, Death Valley was filled by Lake Manly, a perennial saline lake in which 10.3 m of sediment was deposited containing ostracods and subaqueous halite crystal structures from 35 ka to 10 ka. Results from a 185 m core extracted from Badwater Basin and dated using U-series chronologic methods indicate that Lake Manly dried up at 10 ka (Li et al., 1996; Ku et al., 1998; Lowenstein et al., 1999). Death Valley has since remained a "salt pan and saline mud flat" where 7.7 m of mud with a capping layer of primary halite have accumulated (Lowenstein et al., 1999). Shorter cores (3–30 m) extracted using a hand auger in transects across the valley primarily sampled deposits containing brown silt and clay with ~1- to 2-m-thick sand bodies (Hooke, 1972).

METHODS

Our investigation of the Amargosa River, as detailed below, consisted of first mapping channel geometries, measuring erosion rates, and calculating active channel hydraulics based on data from field monitoring. We then used radiocarbon dating of strandline materials and compared calibrated dates to U.S. Geological Survey (USGS) gage data to constrain historic flood frequency and magnitude. Finally, we measured bank grain size using laser diffraction and developed novel laboratory experiments to assess the threshold and rate of bank material erosion during floods.

Channel Mapping, Erosion, and Hydraulics

We selected two bends on the same distributary channel for focused monitoring to observe whether salt crusts dissolved during floods and measure channel geometry changes, erosion rates, and aggradation rates. Monitoring occurred from November 2018 through July 2020, and again in March 2023 after large floods that water year. The primary study site, Bend 1, was located ~1 km north (downstream) of Bend 2, the second site (Fig. 3). Bend 2 had been previously reported to migrate at 1.5 m/yr (Ielpi, 2019).

We directly measured cutbank erosion rates using 51-cm-long erosion pins (Table S1 in the Supplemental Material[1]). We visited sites and measured the exposure of pins installed at two locations with high curvature in Bend 1 and three locations in Bend 2 (Table S1). The pins were pounded flush with the bank upon installation. We measured the length of pin exposed by fluvial erosion on the top and the bottom to millimeter precision and took the mean of these two values to determine erosion between visits before using a hammer to pound the pin flush again with the bank.

Cameras, pressure sensors, and a conductivity sensor collected images and measurements of water stage and conductivity between our site visits. The game cameras took photographs during daytime with a 5 min or 10 min interval. The Onset HOBOware U24-002-C logger measured fluid conductivity and temperature at 10 min

[1]Supplemental Material. Supplemental Texts S1–S2.2, Figures S1–S3, Movies S1–S3, and Tables S1–S4. Please visit https://doi.org/10.1130/GSAB.S.26090536 to access the supplemental material; contact editing@geosociety.org with any questions.

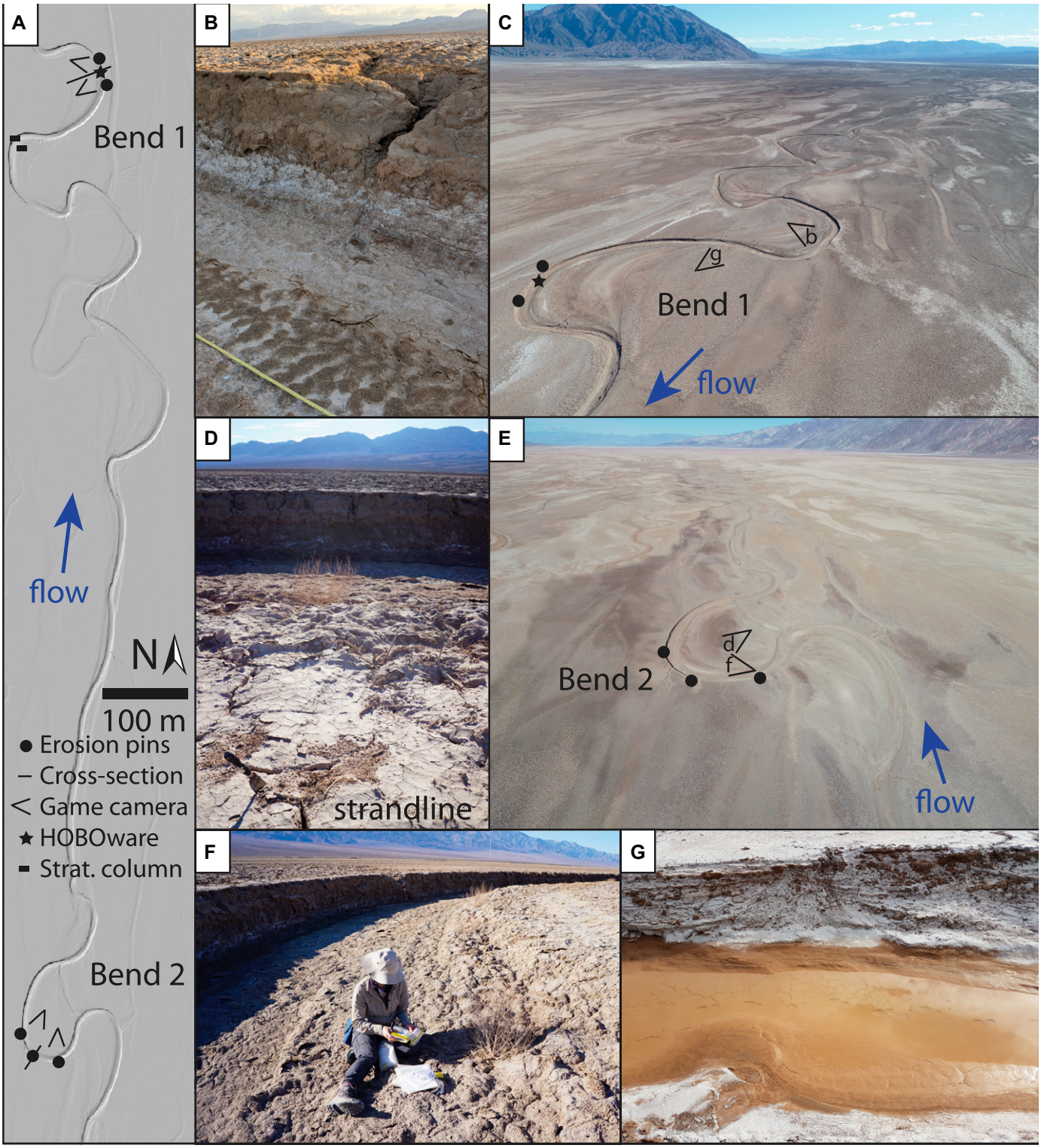

Figure 3. Overview of study bends along active reaches of Amargosa River (Death Valley, California, USA) with downstream flow direction indicated by blue arrows. (A) Lidar hillshade of study areas with measured cross sections (thin line), HOBOware pressure and conductivity sensors (star), erosion pins (circles), game cameras (angle), and measured stratigraphic columns (rectangles) marked. (B) Photo of a shallow, incised channel draining from floodplain into Bend 1 and asymmetric ripples on the channel bed. (C) Aerial image of Bend 1 taken looking south (upstream). (D) Strandline of woody debris and dead vegetation on point bar of Bend 2 that were sampled for radiocarbon dating. (E) Aerial image of Bend 2 looking to the north (downstream). (F) Sampling dead vegetation on point bar of Bend 2. (G) During our visit in January 2019, we observed footprints and mud cracks in a puddle of standing water left by the most recent flood. (Photo taken by Alex Beer.)

intervals to 5 mS/cm and 0.1 °C resolution. Two Onset HOBOware U20L-02 loggers measured water and air pressure (to 1.2 kPa resolution) and temperature (to 0.44 °C resolution). One sensor was attached to a game camera to record air pressure (P_{air}; Pa), and another used to measure water pressure (P_{water}; Pa) was mounted ~5 cm above the channel thalweg to avoid the sensor becoming buried by sediment deposits. We calculated local flow depth (H; m) as

$$H = \frac{P_{water} - P_{air}}{\rho g} + H_{sens}, \quad (1)$$

which depended on the height above the bed of the pressure sensor at the sensor location (H_{sens}; m), fluid density (ρ; kg/m^3), and acceleration due to gravity ($g = 9.81$ m/s^2). We assumed a constant fluid density of 1000 kg/m^3, which introduced less than 1% uncertainty given the range of salinities we measured. We did not monitor in the summer.

To calculate channel hydraulics, we measured channel cross-sectional geometry for each bend with a Trimble R12 Real-Time Kinematic Global Positioning System (RTK GPS) to 1 cm precision. The cross section in Bend 1 included the location where the pressure and conductivity sensors were mounted. From these cross-sectional geometry and water stage measurements, we calculated the wetted top width (B; m), wetted cross-sectional area (A_{xs}; m^2), wetted perimeter (P_w; m), and hydraulic radius ($H_R = A_{xs}/P_w$) by projecting a given water surface elevation across the cross section and using trapezoidal Riemann sums. We then calculated water discharge using Manning's equation:

$$Q_w = \frac{1}{n} A_{xs} H_R^{2/3} \sqrt{S}, \quad (2)$$

where S is channel bed slope. To find bed slope, we traced channel centerlines and fit a line to elevations from 0.5 m resolution lidar collected in 2020 (National Center for Airborne Laser Mapping; OpenTopography, 2020). We used Manning's $n = 0.026$ that we calculated from field measurements during a rare flow event in a very similar nearby channel where we happened to be on site and were able to measure flow discharge directly (Fig. 4; Table S2).

To calculate fluid shear stress on the cutbank, we assumed normal flow conditions and that the stresses on the channel bed and outer bank were similar, such that channel bank stress (τ_{bank}; Pa) was a function of hydraulic radius (Vanoni and Brooks, 1957):

$$\tau_{bank} = \rho g H_R S. \quad (3)$$

This assumption is justified by similar grain size and cm-scale morphological roughness elements (e.g., ripples, mud scours) visible on the channel bed, cutbank, and point bar (see figures cited in "Results"). We defined the shear velocity for the eroding cutbank as

$$u^*_{bank} = \sqrt{\tau_{bank} / \rho}, \quad (4)$$

and used u^*_{bank} in our calibrated sediment entrainment relation (see "Bank Material Characterization and Erodibility") to calculate cutbank erosion rates along our study reach.

In order to evaluate the magnitude of lateral migration across the entire channel network, we determined how many channels were active during the measured floods and if erosion was readily detectable from satellite imagery. We used Planetlabs Planetscope 3 m imagery (Planet Labs, https://www.planet.com/ [accessed 2018]), Landsat 5 30 m imagery from 2009, National Aerial Photography Program (NAPP) 1:40,000 scale imagery from 1995, and National Agriculture Imagery Program (NAIP) 1 m imagery from 2005 to 2020 to map channel cutbanks and centerlines by hand and determine which channels were active during flood events. Active channels had significant color changes due to dissolution and reforming of salt crusts. We drew transects perpendicular to the lower 30 km of the valley centerline and tabulated the number of active versus inactive channels that crossed each transect. We also used Google Earth Pro to replicate the migration rates reported in Ielpi (2019; see Fig. S1; Table S3).

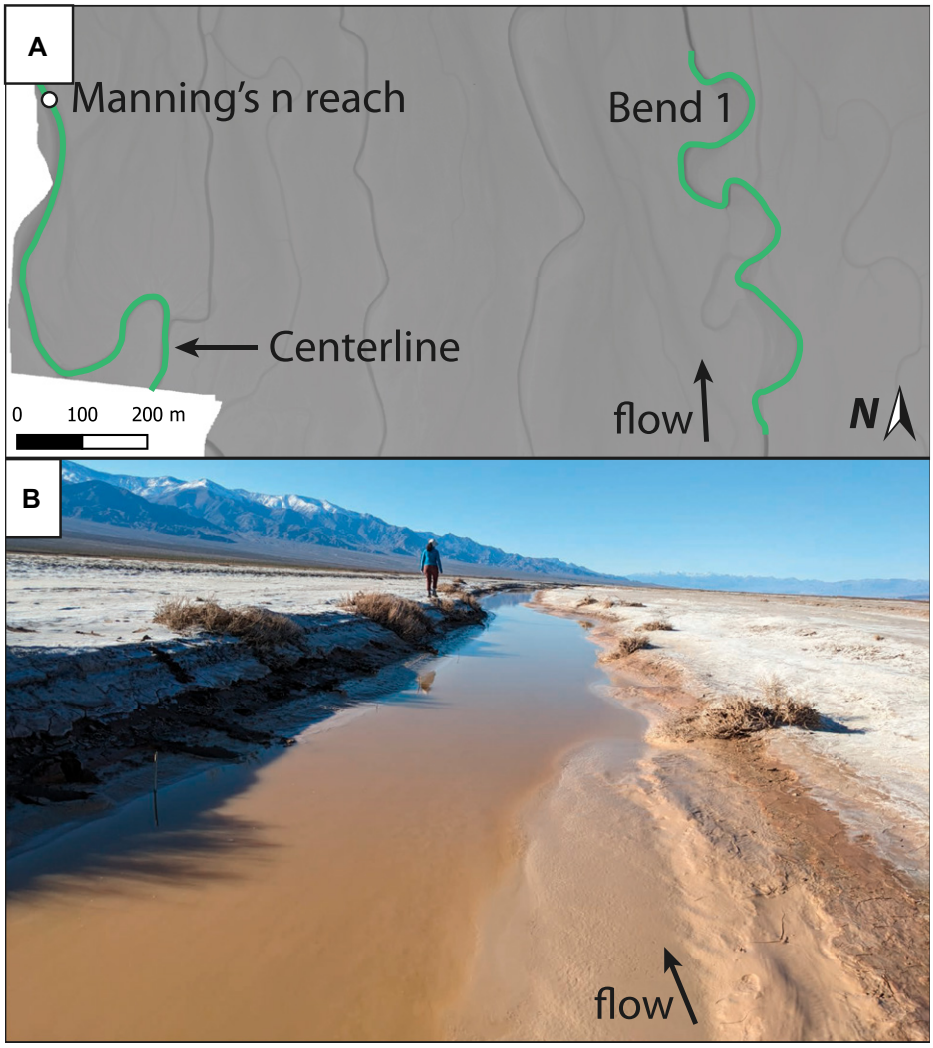

Figure 4. (A) Location of Manning's *n* channel measurement (36.11371203°N, 116.826681°W) in comparison to Bend 1 (Amargosa River, Death Valley, California, USA). Basemap is 0.5 m lidar with channel centerlines used to calculate slope shown in green. (B) Field photo of measurement reach for channel hydraulics used to calculate Manning's *n*.

Historic Flood Frequency

To constrain the flood frequency of the Amargosa prior to our monitoring, we collected samples of plants and woody debris from a strandline on a point bar for radiocarbon analyses. The floodplain of the Amargosa contained sparse deposits of woody debris but almost no plants growing in situ, so this wood originated from vegetation growing many kilometers upstream in the catchment. We selected wood from a continuous strandline at ~1/2 bankfull depth in 2021, prior to the bankfull flood that occurred in 2022. We collected the samples in whirlpaks and rinsed them with MilliQ water before storing them in combusted glass vials and shipping them to the National Ocean Sciences Accelerator Mass Spectrometry Facility at Woods Hole Oceanographic Institution for analysis. To convert from radiocarbon years (BP) to calendar years, we used CaliBomb with IntCal20 and a calibration for Northern Hemisphere Zone 1 to extend the radiocarbon record up to 2020 (Reimer et al., 2013; Hua et al., 2022; Reimer and Reimer, 2023).

We used long-term hydrologic datasets for the lower Amargosa to calculate flood magnitude and frequency over decadal time scales. The closest upstream river gage with a long period of record was located 60 km to the southwest at Tecopa, California (USGS 10251300), with a discontinuous record beginning in 1962 and a continuous record from 1998 to present. The closest rain gage was located 39 km north in Furnace Creek, California (National Weather Service Global Historical Climatology Network Daily USC00042319), with continuous records from 1961 to present. Both gages were far from our study site but provided an opportunity to calibrate a relation between the gages and discharge in our study reach.

Bank Material Characterization and Erodibility

To characterize floodplain material at Bend 1, we dug two trenches (2.2 m and 6.5 m long) in the point bar perpendicular to flow direction and measured ten stratigraphic columns, as well as recorded seven cutbank stratigraphic columns and two for pits dug into the channel thalweg. At Bend 2, we measured two stratigraphic columns on the cutbank, one on the point bar, and recorded five along other reaches of the river. All stratigraphic columns had 1 cm resolution, and we measured sediment grain size using a grain size card and a hand lens. We also collected samples for grainsize analysis and analyzed them using laser diffraction in a Malvern Mastersizer 3000 following a standard, previously described protocol (Gee and Or, 2002; Douglas et al., 2022).

To test whether mud entrainment alone was the rate limiting step to cutbank erosion, we used sampled bank material in a physical experiment to measure its erodibility (Figs. 5A and 5B). The setup was based on previous experimental work in abrasion mills (Sklar and Dietrich, 2001; Scheingross et al., 2014; Trower et al., 2017). To avoid unnecessary disturbance of the bank sample, we detached the 20-cm-diameter cylindrical portion of the mill and brought it to the field site to directly sample the base of the cutbank (Fig. 5A). We removed salt crusts from the bank to expose the underlying muddy sediment and used a sledgehammer to pound the cylinder into the base of the bank and collect a 10-cm-deep sample of intact riverbank.

In the lab, the mill was filled to 40 cm depth with saline solution produced by dissolving salt crusts from the sampling site in tap water to a conductivity of ~30,000 µS/cm, which was representative for floods in the Amargosa. We ran the experiment by setting the spin rate of the flat plate driving fluid flow at the top of the mill using a variable frequency drive, which was calibrated in terms of shear velocity (Supplemental Text S1; Fig. S2; Table S4). The experiment pro-

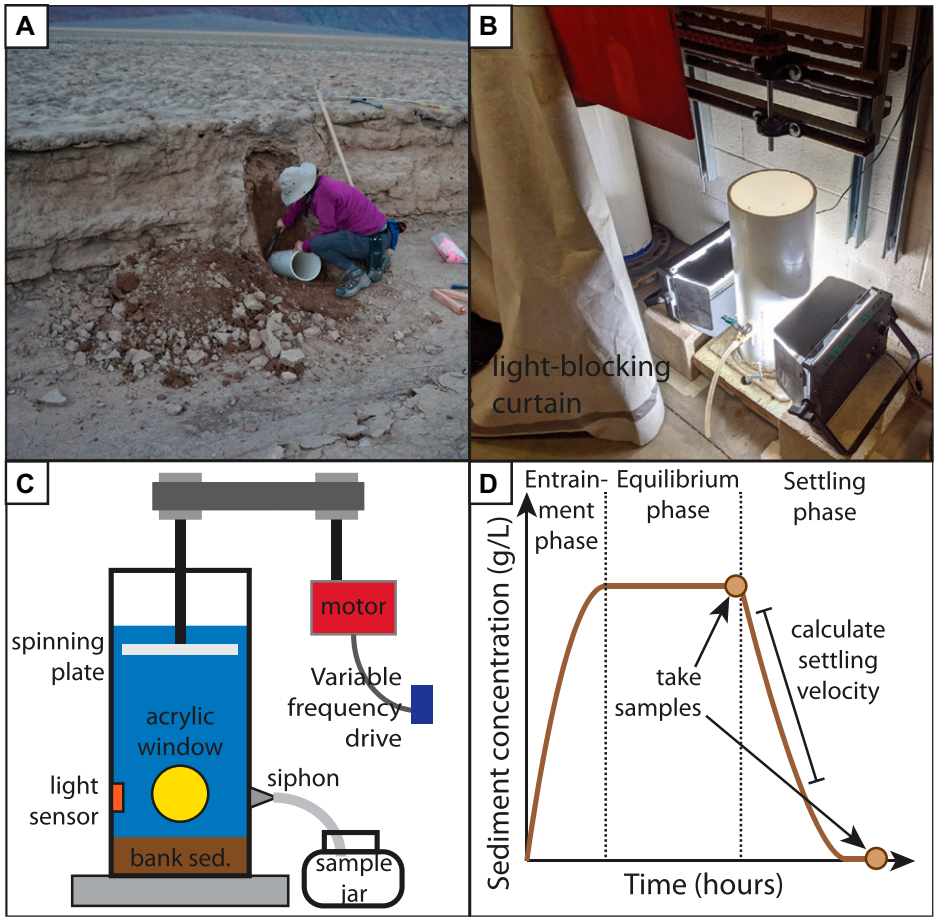

Figure 5. Sampling and experimental setup and results from abrasion mill tests on Amargosa River (Death Valley, California, USA) bank sediment. (A) Digging out a PVC pipe that was pounded into the bank of the Amargosa River to collect intact riverbank sediment. (B) Photo of experimental setup, where spotlights are shown through acrylic windows installed in the side of the PVC pipe and the setup is covered by a light-blocking curtain. (C) Cartoon cross section of experimental setup, where a variable frequency drive sets the speed of a motor that turns a spinning plate. This exerts shear on the bank sediment (sed.), picking up sediment that obscures light shining in through an acrylic window. Measurements of sediment concentration were made indirectly using a light sensor and directly by siphoning fluid into a glass jar. (D) Cartoon time series of expected measured sediment concentration (g/L) data during the entrainment, equilibrium, and settling phases of an experimental run, displaying times when fluid samples were collected and the sediment settling velocity calculated.

TABLE 1. ABRASION MILL EXPERIMENTAL PARAMETERS AND GRAIN SIZES FROM SIPHONED SAMPLES AT THE END OF EACH STAGE

Stage	Sediment concentration (g/L)	Water conductivity (mS/cm)	Suspended sediment D_{10} (μm)	Suspended sediment D_{50} (μm)	Suspended sediment D_{90} (μm)	Rotations per minute (RPM)	Shear velocity (m/s)
Initial bed	N.D.	N.D.	0.832	8.608	35.659	0	0
1	0.75	30.4	0.643	4.901	19.747	124.5	0.016
2	1.05	29.7	0.433	4.386	20.312	152.1	0.017
3	0.69	30.6	0.664	5.890	23.198	177.9	0.018
4	2.45	31.6	0.717	5.676	22.668	199.5	0.019
5	9.38	33.0	0.557	5.058	21.867	227.8	0.020
Final bed	N.D.	33.2	2.448	9.977	430.921	0	0

Note: N.D.—no data.

gressed through a series of stages that consisted of stepwise increases in shear velocity (Table 1). For a given stage, the sediment concentration first increased (entrainment phase) and eventually stabilized (equilibrium phase) as the entrainment and settling fluxes balanced (e.g., Garcia and Parker, 1991). During the equilibrium phase for each stage, we measured fluid conductivity with a handheld probe and collected ~1 L of turbid water via the spigot and siphon tube in the side of the mill (Figs. 5B and 5C). We replaced the saline solution after each sample before proceeding to the next stage. In the final stage (settling phase), we set $u^* = 0$ m/s and let the suspension settle in still water. At the end of the experiment, we took a water sample to determine the salt concentration. We sampled the bed at the beginning and end of the experiment for grainsize analysis.

During the experiment, we measured turbidity as a proxy for sediment concentration every 10 seconds using a light sensor (Onset HOBOware MX Temp/Light Pendant with HOBOconnect application) mounted to the inside of the mill at 10 cm above the sediment bed. Two windows at 90° and 270° from the light sensor flooded the mill with light (Figs. 5B and 5C). The light sensor was calibrated to suspended sediment concentration measured to 0.1 g/L precision from the water samples taken at the end of each equilibrium phase (see Supplemental Text S2.1; Fig. S3). Samples taken during the experiment were weighed and dried to measure the salt and sediment concentrations. We confirmed that the grain size of suspended sediment was not changed throughout the experiment by measuring siphoned samples on the Malvern Mastersizer 3000.

To calculate the sediment entrainment fluxes, we analyzed the measured sediment concentrations from the calibrated light sensor. From conservation of mass, the change in the total sediment concentration, c (g/L), was equal to the vertical sediment entrainment flux minus the settling flux (Garcia and Parker, 1991),

$$\frac{d}{dt}\int_0^{H_m} c(z,t)\,dz = E - c_b w_s, \tag{5}$$

where H_m (m) is the depth of water in the mill, E (g × m/L/s) is the sediment entrainment rate from the bed, c_b (g/L) is the near-bed sediment concentration, and w_s (m/s) is the sediment settling velocity. We assumed a dilute suspension of sediment, flat channel bed, constant settling velocity, and that the suspended sediment was well-mixed, such that $\frac{1}{H_m}\int_0^{H_m} c(z,t)\,dz = c_b = \overline{c}$, where $\overline{c}$ (g/L) is the average sediment concentration. The well-mixed assumption was justified by the very small Rouse number ratio of $w_s/\kappa u^* < 0.02$ (Supplemental Text S2; Rouse, 1937), where κ is the von Kármán constant. From Equation 5, the equilibrium phase of each experiment stage was used to measure the entrainment rate of sediment from the bed, i.e.,

$$E = \overline{c} w_s, \tag{6}$$

where we measured $\overline{c}$ at steady-state as $c_{m,ss}$, the steady-state value of the well-mixed concentration measured by the light sensor.

To find the settling velocity needed in Equation 6, and since flocculation may have occurred, we took advantage of the settling phase of the experiment. During this phase, the suspended sediment settled at the settling flux $c_{m,ss}w_s$, forming a settling interface with turbid water of concentration $c_{m,ss}$ below and clear water with negligible suspended sediment above. As this settling interface moved through the light sensor measurement volume, the sensor measured this change as an average over the measurement volume of height D; so that $c_m = \frac{1}{D}\int_{z_D-0.5D}^{z_D+0.5D} c(z,t)\,dz$, where $z_D = 10$ cm was the height of the sensor. Thus, by mass balance

$$\frac{d}{dt}\left(\int_{z_D-0.5D}^{z_D+0.5D} c(z,t)\,dz\right) = \frac{d}{dt}(c_m D) = -c_{m,ss}w_s \tag{7}$$

during the time interval when the settling interface passed through the measurement volume. Integration of Equation 7 yielded

$$c_m(t) = c_{m,ss}\left(1 - \frac{w_s t}{D}\right) \tag{8}$$

after applying the boundary condition $c_m(t = 0) = c_{m,ss}$ where $t = 0$ was when the settling front is located at height $z_D + D/2$. We set D equal to the diameter of the windows (8.6 cm) that let light into the mill. We fit Equation 8 to our data of $c_m(t)$ during the settling phase to find $w_s = 1.51 \times 10^{-4}$ m/s. We substituted the measured w_s and $c_{m,ss}$ into Equation 6 and solved for the sediment entrainment rate E during each equilibrium phase. The model was validated against the data during the entrainment phase, which was not used in model calibration, by inserting E and w_s into Equation 5 to solve for $c_m(t)$ throughout the entrainment, equilibrium, and settling phases.

RESULTS

Channel and Planform Morphology

As it traverses the floor of Death Valley, the Amargosa River divides into a network of distributary channels (Fig. 6). Changes in salt extent visible in satellite imagery indicate that most channels across the floodplain are active (Figs. 6A and 6B). Both the number of channels and proportion of active channels decreased approaching Badwater Basin (Fig. 6C). Inactive channels tended to cluster near the center of the valley, farthest from the bounding faults on its east and west edges.

Numerous shallow channels run parallel or radiate from deep, active river bends (Figs. 6D–6H). For example, Bend 2 had a shallow channel connecting the bend across its point bar and another shallow channel radiating from the upstream portion of the bend that appeared to flow into a floodplain secondary channel (Fig. 6E). Here, we inferred the river might decelerate as flow turned up-valley, causing the river to overtop its bank and begin to form a chute cutoff as well as overbank flow to a previously abandoned floodplain channel.

The floodplain surrounding Bend 1 had similar characteristics to that near Bend 2: a shallow

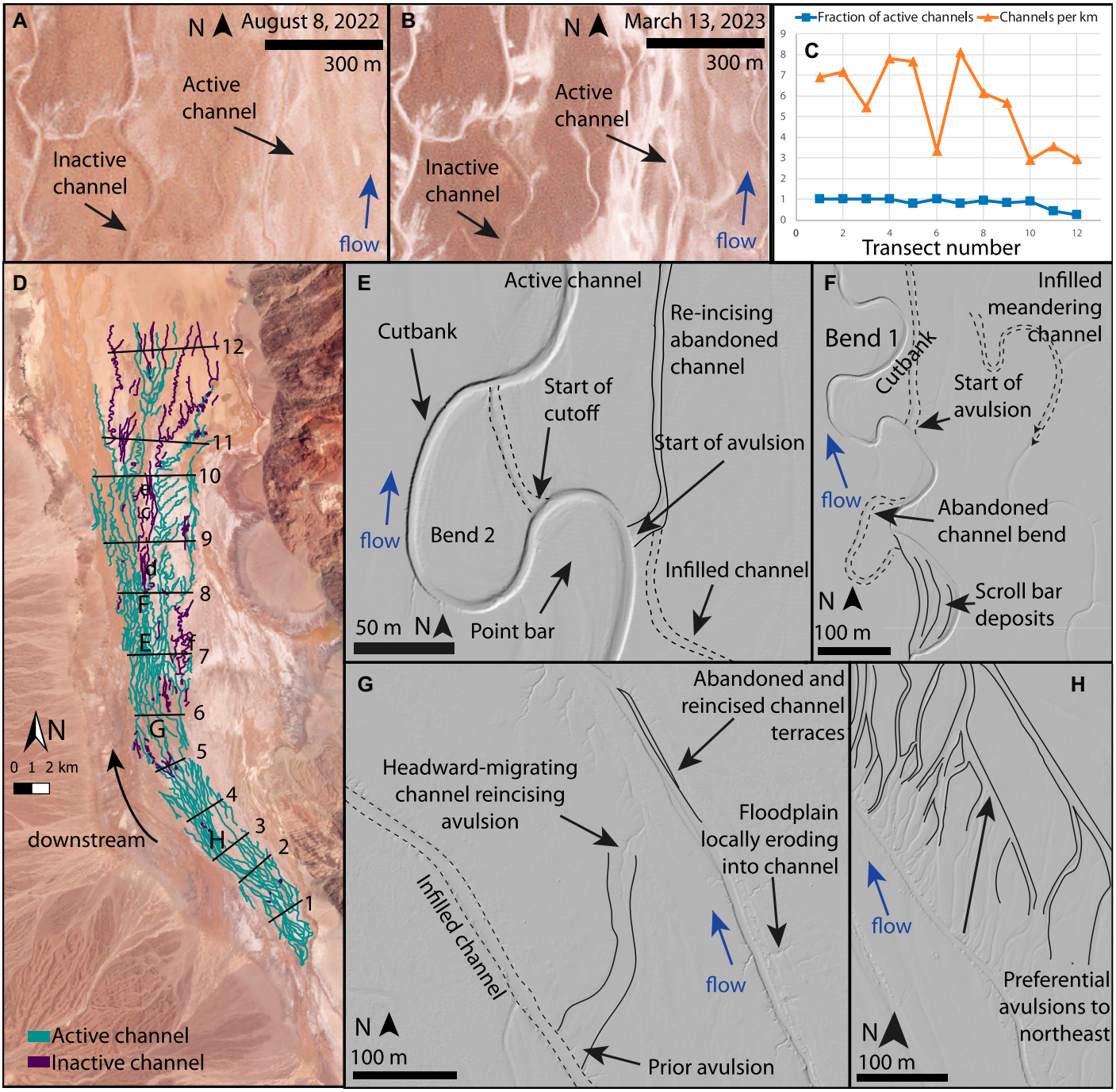

Figure 6. Active channels show changes in salt crust patterns during floods (Amargosa River, Death Valley, California, USA). Between (A) 8 August 2022 and (B) 13 March 2023, active channels became covered in white salt while inactive channels experienced no visible changes. (C) The fraction of active channels intersecting each transect (orange triangles) and number of channels per km distance (blue squares) along each transect. (D) Planetlabs 3 m satellite imagery of Death Valley in August 2022 overlain with traces of active (teal) and inactive (purple) channels traced by hand from lidar imagery (Image ©2023 Planet Labs PBC). Active channels showed significant change in ground color and salt crust distributions between the start and end of August 2022, when a significant flood event occurred. Transects where channel statistics were measured are shown as numbered black lines and the locations for panels (E) through (H) are indicated with the panel letter. Lidar hillshade topography of characteristic floodplain features along the Amargosa River for our two study sites. (E) Bend 2 (map lower right corner at 36.103°N, 116.813°W), and (F) Bend 1 (map lower right corner at 36.110°N, 116.812°W) with channel flow directions shown by a blue arrow. (G) Example of shallow channels on the floodplain with secondary channels incising their banks (map lower right corner at 36.060°N, 116.803°W) with channel flow directions shown by a blue arrow. (H) Secondary channels flowed preferentially to the northeast (map lower right corner at 36.032°N, 116.785°W) with channel flow directions shown by a blue arrow.

channel flowing parallel downstream to the east, a neck cutoff that left a shallow and presumably infilled channel reach, and shallow channels radiating from locations where flow turns perpendicular or up the valley axis. From these observations, we inferred a multi-stage history for Bend 1 (Fig. 6F). First, the channel avulsed at an upstream location, abandoning the eastern meanders, which subsequently were filled in by floodplain material. Then, the active channel increased its sinuosity, producing scroll bars. When the channel became sufficiently sinuous that the river decelerated and overtopped its bank, the overbank flow was directed back into the active channel. This formed a cutoff and abandoned channel bend, which was then slowly infilled. At the time of the lidar survey, the bend downstream of the cutoff (Bend 1) was highly sinuous and had begun overtopping its bank during high flows and incising a channel that could grow to form a distributary channel or trigger an avulsion eastward.

In Figure 6G, the western channel was shallow, with a symmetric, flat bed and numerous short gullies along its edge. We interpreted this feature as an abandoned channel that was slowly being infilled by floodplain sediment and erosion of its banks by direct rainfall. The channel to the east had a similar morphology but with a narrow inner channel with steep banks (Fig. 6G). This channel might have been abandoned, infilled, and subsequently re-occupied and incised. Field observations show these shallow, active channels on the floodplain appeared to grow via headward incision, providing a mechanism for these shallow channels to capture a larger fraction of stream discharge and eventually abandon the original channel, completing an avulsion cycle.

In general, avulsions and overbank floods preferentially produced new channels flowing to the northeast. In some locations, numerous shallow channels radiated from the eastern bank of an active channel, joined, and then incised a deeper flow path (Fig. 6H). The eastern bounding fault of Death Valley is slipping more rapidly than the western fault, causing the valley to slowly tilt to the east (Hooke, 1972). Thus, the preferential flow direction was likely caused by the Amargosa avulsing toward the axis of maximum subsidence, then migrating back toward the center of the valley due to the sediment supplied by alluvial fans along the Black Mountains (Kim et al., 2011; Kopp and Kim, 2015).

Our study reach contained actively meandering channels that produced similar landforms as perennial meandering rivers. Bends 1 and 2 formed asymmetrical channels with steep erosional cutbanks that expose floodplain stratigraphy and low-gradient sandy point bars (Figs. 6E and 6F). The channels had scroll bar patterns, sinuosities, and width-to-depth ratios

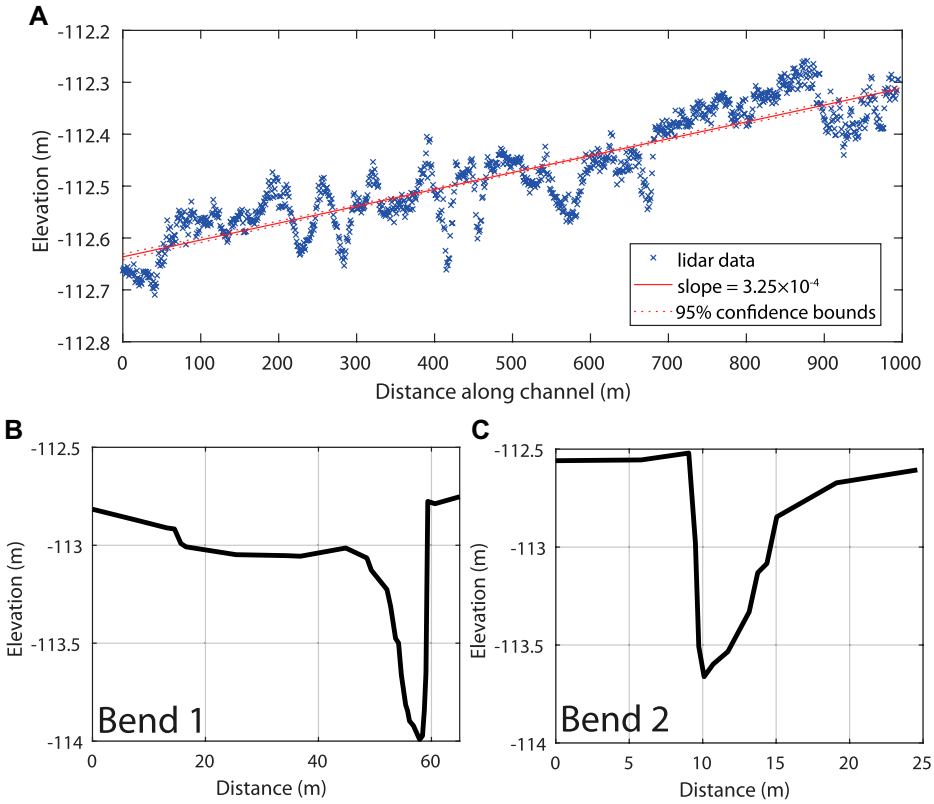

Figure 7. (A) Lidar elevation of channel centerline from Bends 1 and 2 (Amargosa River, Death Valley, California, USA) in our study reach, and the linear least squares regression used to calculate channel slope as a function of distance along the centerline (red dashed line). (B) Channel cross section at Bend 1 surveyed using RTK GPS, 1SD measurement uncertainty (1 cm) within line thickness. (C) Cross section of Bend 2 surveyed using RTK GPS, 1SD measurement uncertainty within line thickness.

similar to vegetated meandering channels (Ielpi, 2019). Similar to vegetated meandering rivers, channel slope was low ($S = 3.25 \times 10^{-4}$) and varied along the longitudinal profile (Fig. 7A). The channel thalweg was deepest at the apex of each bend, where it was located close to the cutbank and the point bar had a shallow slope (Figs. 7B and 7C), while the channel had a symmetric cross section and shallow thalweg at the inflection point between bends. These observations coupled with erosion rates measured from satellite imagery following Ielpi (2019) indicate that reaches of the Amargosa are actively meandering.

Floodplain and Channel Sedimentology

Cutbanks contained sedimentary beds ~10 cm thick composed primarily of silt with stringers of clay and cross-bedded very fine sand (Fig. 8A). The cutbank slightly coarsened upward from silt with clay stringers to laminated silt and very fine sand, and the uppermost layer of the bank consisted of a 10-cm-thick salt crust, which also coated the eroding face of the riverbank (Fig. 8). These deposits were generally finer-grained than material being deposited on point bars (Figs. 8B–8D).

The upper 5 cm of the thalweg bed material consisted of thin beds of alternating silt and very cohesive clay that overlay sandy deposits. We attributed the fine capping deposits to water ponding in the channel thalweg as it dried between floods, causing clay typically transported as washload to be deposited in these locations. These thin clay layers may armor the channel bed and prevent sediment motion during low flows, since we observed a footprint and mud cracks in January 2019 left from a previous trip that survived flow through the channel in the meantime (Fig. 3G). Between floods, the channel bed and point bar developed a surficial layer of crystallized salt that formed hummocky textures or a thin crust on mud cracks but did not form thick salt crusts like those present on the cutbank. Point bars were primarily composed of very fine sand with centimeter-scale climbing ripple cross-stratification, char-

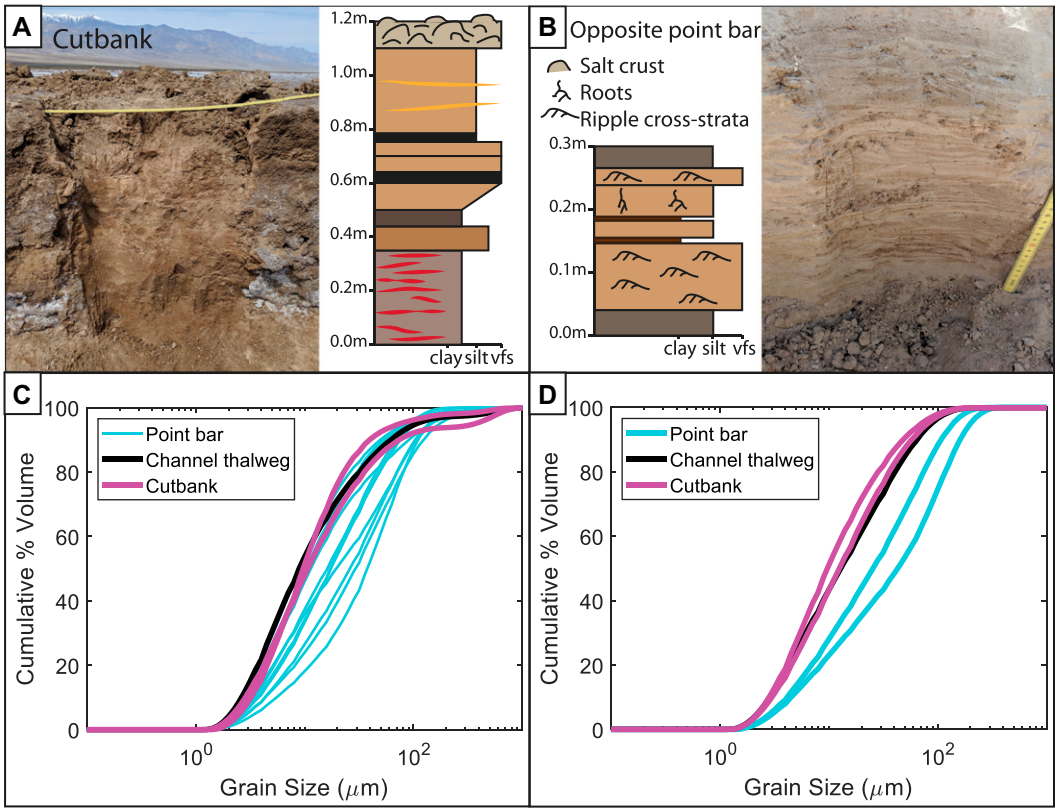

Figure 8. Field photographs of stratigraphic columns from cutbank (A) and point bar (B) (Amargosa River, Death Valley, California, USA). Location of stratigraphic columns is marked on Figure 3. (C) Grain size measured using laser diffraction for two cutbank samples (magenta lines), two thalweg samples (black lines), and 11 point bar samples (thin blue lines) in Bend 1. (D) Grain size measured using laser diffraction for two cutbank samples (magenta lines), one thalweg sample (black line), and two point bar samples (blue lines) from Bend 2.

acteristic of active point bars. Salt crusts were not visible below the surficial layer of point bar and thalweg deposits.

Both bends had very sparse vegetation on their point bars, few roots were visible in point bar stratigraphy, and no plants or roots were visible in cutbanks (Fig. 8). Radiocarbon dating indicated the plants likely grew following high flows in 2015 (Table 2). Wood was also present in a strandline, but radiocarbon ages ranged over hundreds of years, implying the wood had been stored in the catchment before being transported downstream.

TABLE 2. RADIOCARBON DATING RESULTS AND CONVERSION TO CALENDAR AGES

Fraction modern (Fm)	Calibrated dates (% probability)	Most probable dates (AD)
DEVA-Plant1		
1.0162 ± 0.0021	2016.82–2018.11 (85.1%) 2018.54–2018.70 (9.0%) 2016.24–2016.32 (4.3%) 1955.45–1955.48 (1.6%)	2015–2018
DEVA-Plant2		
1.0184 ± 0.0022	2016.06–2017.01 (64.3%) 2017.43–2018.05 (24.8%) 1955.46–1955.66 (10.9%)	2015–2018
DEVA-Plant3		
1.0156 ± 0.0025	1989.88–1990.29 (76.4%) 2018.49–2018.77 (15.7%) 1955.39–1955.50 (5.3%)	2015–2018
DEVA-Strandline1		
1.1596 ± 0.0022	1989.88–1990.29 (76.4%) 1958.64–1958.84 (23.6%)	1989–1990
DEVA-Strandline2		
0.9762 ± 0.0020	1763.73–1785.21 (35.7%) 1663.78–1679.02 (24.8%) 1740.98–1751.68 (16.4%) 1794.09–1799.00 (8.6%) 1944.67–1949.60 (7.3%) 1942.21–1944.29 (3.1%) 1950.03–1951.79 (2.4%) 1952.28–1953.07 (1.2%)	1664–1668
DEVA-Strandline3		
1.3811 ± 0.0027	1975.07–1975.30 (72.0%) 1975.80–1975.88 (20.5%) 1962.40–1962.43 (7.5%)	1974–1975

Note: Calibrated dates were calculated using 1SD uncertainty on the measured radiocarbon fraction modern. We report all calibrated dates with >1% probability.

Flood Monitoring

Our monitoring documented three flow events, which were uncorrelated with rainfall at Furnace Creek (Fig. 9A) but all coincided with peaks in the discharge measurements at Tecopa (Figs. 9B and 9C). River discharge (calculated using Equations 2–4) decreased between Tecopa and our study site by approximately a factor of five, likely because water infiltrated and evaporated as it flowed downstream and because a portion of flow was routed through other channels on the floor of Death Valley (Fig. 9C). We measured high river water electrolytic conductivity that varied between and throughout floods (Fig. 9D). Calculated bank shear velocities increased with flow discharge (Fig. 9E).

We directly measured ~8 cm of erosion at the cutbank in Bend 1 below the high waterline using erosion pins. The erosion primarily occurred 12–15 March based on game camera footage (Fig. 10). The flood began at night, with muddy water visible in the channel at dawn

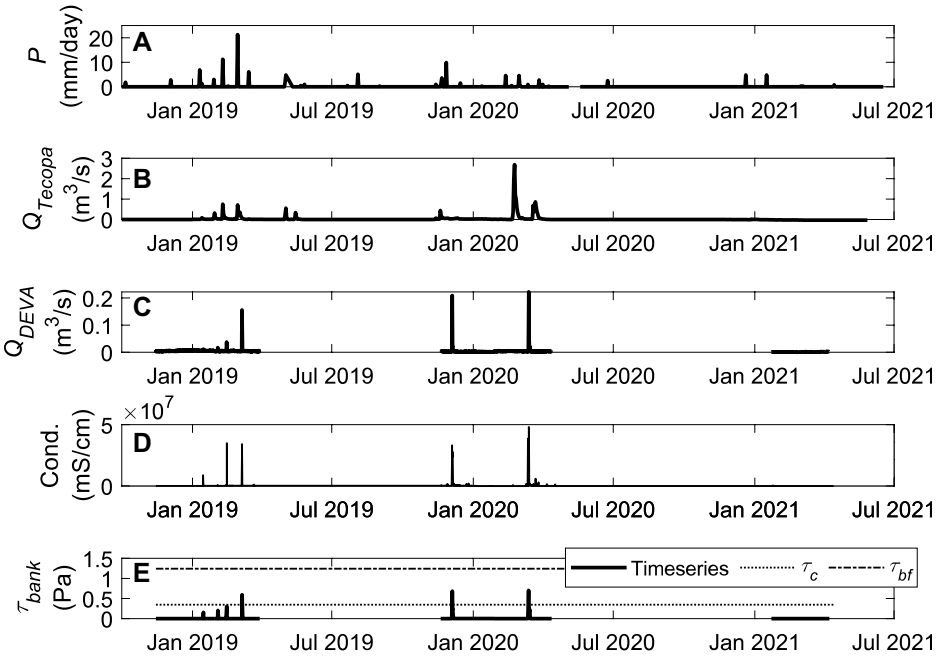

Figure 9. Time series of hydraulic measurements from November 2018 to July 2021. (A) Rain gage at Furnace Creek, California, USA. (B) Water discharge measured by U.S. Geological Survey stream gage 10251300 in Tecopa, California. (C) Water discharge calculated using Manning's equation and measured flow depths and cross-sectional geometry for our study reach. (D) Fluid conductivity measured with at same location as stage height. (E) Fluid shear velocity time series on the channel banks at our study reach (solid line), with critical shear stress for entrainment determined from experiments (*τc*, dotted line) and the channel bankfull shear stress (*τbf*, dashed line) shown for comparison.

(Fig. 10B). As the water receded, it left a niche where salt crust dissolution and bank erosion occurred (Fig. 10C). We measured little erosion on the upper portions of the riverbank, though we observed slump blocks neighboring the erosion pins with diameter ~10 cm failing in game-camera timelapse footage (Movie S1). As the flood receded, water stagnated in the pool at the apex of the bend and surficial salt crusts crystalized (Figs. 10A and 10 D). Erosion pin measurements documented that these sub-bankfull flows exceeded the threshold for bank sediment entrainment and caused cutbank erosion.

A larger, bankfull flood occurred in September 2022, which we captured using erosion pins, though we had ceased using game cameras and HOBO loggers at that time (Fig. 11A). Lacking water stage measurements, we determined that the maximum flow depth reached bankfull conditions from a strandline of woody debris present at the top of the cutbank and high on the point bar, as well as overhanging salt crusts extending immediately above the strandline (Fig. 11). The strandline provided a lower bound on the high-water line and the overhanging salt crusts were not inundated, so these markers bracketed the maximum flood stage. This flood caused significant bank erosion, on average 18.5 cm from the 10 erosion pins, and completely eroded one 51-cm-long erosion pin from the bank (Fig. 11C). Repeat RTK GPS cross-sectional surveys indicate that the river widened slightly, experiencing 7 ± 3 cm (±1SD) of aggradation on the point bar and channel bed (Fig. 11B), supported by measurements of 7.5 cm deep mud cracks formed around plants buried by mud (Fig. 11D). We also observed mud rip-up clasts that had been transported as bedload in the river, implying that cohesive mud limits erosion of channel bed and point bars as well as the cutbank (Fig. 11C). Aggradation of the channel bed may have accounted for lower erosion rates measured from erosion pins at the lower part of the bank (Table S2).

After the flood, previously inundated portions of the floodplain were coated with a fresh thin layer of bright white salt highlighting where the Amargosa overtopped its banks at Bends 1 and 2 (Fig. 11). Much of the upper layer of salt crusts had been dissolved across the floodplain, presumably by overbank flow or direct rainfall. Banks were typically overhung, with the strandline below bankfull, when flow in the bend was directed downvalley. As the bends curved to flow across or up the valley, the strandline approached the top of the bank, the series of overhangs ended, and eventually the strandline disappeared, and fresh salt was visible extending from the channel onto the floodplain, signifying overbank flow (Fig. 11F).

The banks of the Amargosa were coated with decimeter-scale thick salt crusts, which covered the underlying muddy sediment (Fig. 12A). However, we observed that the salt crusts completely dissolved during flow events in channels near Bend 1 (Fig. 12C). At the base of the bank, the salt crusts fully dissolved and erosion pins protruded through fine sediment with mud cracks coated in a thin veneer of fresh salt (Fig. 12B). This indicated that the river was able to directly mobilize mud. Conductivity sensor measurements supported that salt was completely dissolved during flow events because water conductivity varied significantly within each event (Fig. 12D). We would have expected conductivity to remain relatively constant if the water instead became saturated with salt and was not able to dissolve the crusts on its banks. From these lines of evidence, we inferred that salt crusts fully dissolved during floods and did not supply the primary cohesive force to enable channel meandering.

Cutbank Entrainment Measurements

We analyzed data from the equilibrium and settling phases of the mill experiment to determine sediment entrainment rates and the threshold of entrainment. In each entrainment phase, the sediment concentration began to increase immediately after shear velocity was increased and the experiment entered the equilibrium phase when sediment concentration stabilized after ~2 h (Equation 6; Fig. 13A). Higher shear velocity caused a nonlinear increase in equilibrium sediment concentration—with large jumps between $u^* = 0.018$, 0.019, and 0.020 m/s—as well as an increase in the time required for the concentration to stabilize. For $u^* = 0.020$, the concentration curve became discretized as it approached the resolution of the light sensor. In the settling phase, sediment concentration remained constant for a short period after we set $u^* = 0$ m/s, then abruptly declined to less than 1 g/L, before slowly declining to 0 g/L after 2 h (Fig. 13B). This trend in concentration supported our assumption that particles had roughly the same w_s so that sediment settled as a uniform front, with the rapid decline occurring as the front passes the acrylic window where light shined through to the sensor. The subsequent slow decline was then from any remaining fine sediment settling from the column, which had a very slow settling velocity.

Differences in the measured settling velocity from the theoretical Stokes settling velocity

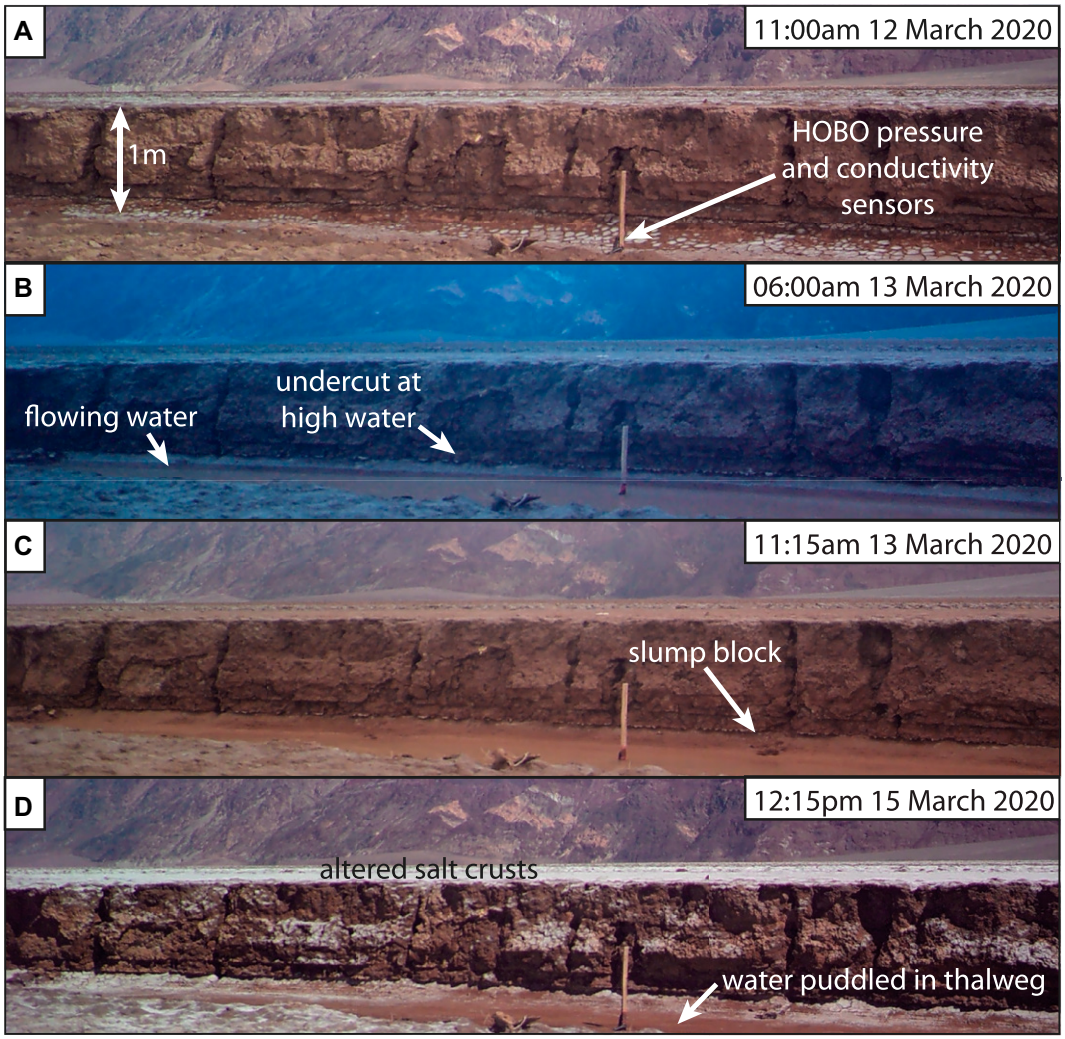

Figure 10. Game camera timelapse images of Bend 1 before (A), during (B, C), and after (D) a flood from 12 to 15 March 2020 (Amargosa River, Death Valley, California, USA). HOBO—data loggers used in study.

indicated that suspended sediment was slightly flocculated during the experiments (Zeichner et al., 2021). We found $w_s = 1.51 \times 10^{-4}$ m/s (Equation 9), which corresponded to an effective siliciclastic grain diameter of 13.9 µm (Dietrich, 1982). For comparison, the final experimental bed had median grain size $D_{50} = 9.98$ µm, giving a predicted settling velocity of 7.39×10^{-5} m/s (Table 1; Dietrich, 1982)—approximately two times faster than the experimental settling velocity, though these differences could be due to grain shape. Therefore, we used the measured w_s to calculate sediment entrainment rates (Equation 6).

Next, we used experimental data to calibrate an erosion relation for bank sediment in the meandering section of the Amargosa River. Standard erosion relations pose that E_{expt} (mm/hr) is linear function of excess shear stress (Partheniades, 1965), where E_{expt} is a function of entrainment rate E (g × m/L/s) divided by sediment density (2650 kg/m^3 = 2650 g/L). We observed some sediment entrainment at very low shear velocities and then a rapid increase in sediment entrainment past an apparent threshold shear velocity around ~0.018 m/s (Fig. 13C). Therefore, we fit different linear functions for the nearly flat and steeply increasing portions of the sediment entrainment curve, such that

$$E_{expt} = \begin{cases} 0 & \tau < 0.58\tau_c \\ 0.64\tau / \tau_c - 0.37 & 0.58\tau_c < \tau < \tau_c \\ 11.5\tau / \tau_c - 11.23 & \tau \geq \tau_c \end{cases}, \quad (9)$$

where the linear coefficients and intercepts have units of mm/hr. We identified the threshold shear velocity for significant entrainment as the intersection of these two lines, which occurred at $\tau_c = 0.35$ Pa, and set the entrainment function to zero for $\tau < 0.58\tau_c$. The nonzero entrainment rate for $0.58\tau_c < \tau < \tau_c$ was likely due to disturbed mud aggregates at the surface of the mill with grains that did not completely settle or compact, similar to the experiments of Partheniades (1965).

ANALYSIS

In this section we first use field surveys, erosion pin measurements, and laboratory measurements of bank erosion rates to validate our bank erosion equation (Equation 9). We then develop a discharge relation between our study site and the USGS Tecopa gage (Equation 10) and use this relation to calculate flood frequencies and erosion rates over decadal time scales. Finally, we use these erosion rates and published aggradation rates to calculate a channel mobility number and determine the floodplain stratigraphic architecture.

Comparing Erosion between Laboratory and Field

We used the experimental model for bank erosion and surveys of channel geometry to calculate expected erosion rates and compared them to field measurements of erosion rate to evaluate if mud was the dominant bank strengthening agent. We applied our experimental sediment entrainment

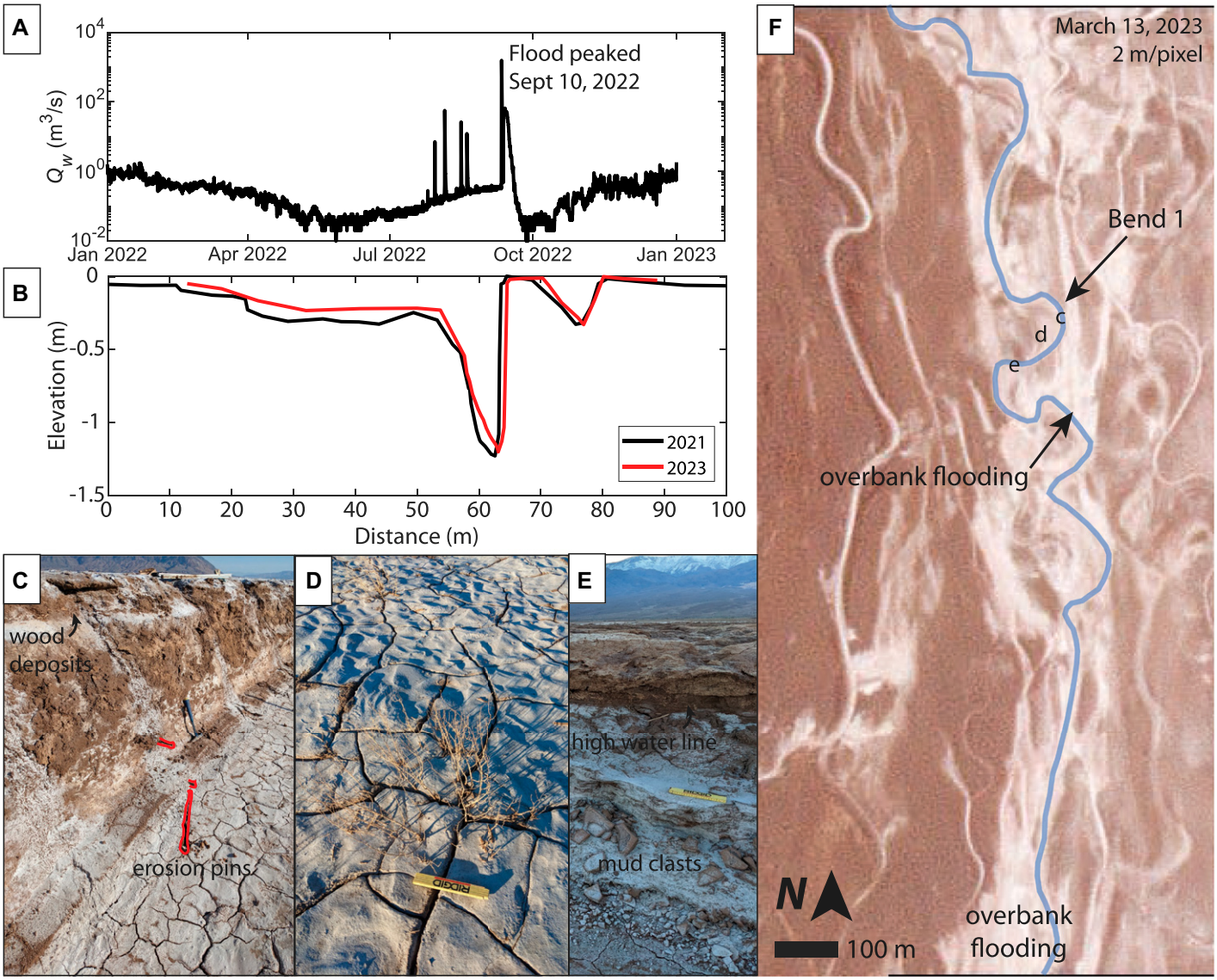

Figure 11. Field photos and remote observations following summer 2022 bankfull flood (Amargosa River, Death Valley, California, USA). (A) U.S. Geological Survey gage at Tecopa (California) records of 15 min average discharge for 2022. (B) RTK GPS measurements of channel cross section at Bend 1 along the same transect from 2021 (black line) and 2023 (red line). (C) Erosion pins (outlined in red) and woody debris strandline at cutbank in Bend 1. (D) Plant buried by 7.5 cm of mud on point bar of Bend 1. (E) High-water line marked by woody debris and mud clasts being eroded out of Bend 2. (F) Satellite imagery (2 m/pixel) taken on 13 March 2023 (Image ©2023 Planet Labs PBC). The study reach is drawn in blue, and overbank deposits are visible as white salt deposits on the brown floodplain.

rate (Equation 9) to the floods that occurred when we had river stage records. We set $\tau_{bank} = 0$ for cases when the fluid shear velocity (calculated using Equations 4 and 5) was below τ_c or the water depth was shallower than the height of the erosion pins above the bed. We used these water stage measurements and surveyed channel cross-sectional geometries and bed slopes to evaluate Equations 2–4 and calculate near-bank fluid shear velocities throughout the floods. Modeled entrainment from two discrete floods agreed with erosion pin measurements over the same interval (Fig. 14A), indicating that our laboratory calibration of bank sediment entrainment rates produced accurate bank erosion rates under field conditions.

We used flood stage markers from the strandlines and overhangs to determine the peak flood stage and estimate bankfull shear velocities for the 2022 bankfull flood. We found that bankfull flows had $\tau_{bank} = 1.24$ Pa, above the threshold of significant mud erosion (from experiments, $\tau_c = 0.35$ Pa) by a factor of 1.6, with predicted bankfull erosion rates of 30 mm/hr (Fig. 5F). During the bankfull flood, we observed a maximum of >51 cm of erosion for one pin located 20 cm below the top of the cutbank, likely due to a slump block collapse at this location. Excluding this maximum erosion measurement, the other erosion pins averaged 18.2 ± 6.1 cm (mean ± standard deviation) of erosion during the bankfull flood. This amount of erosion is equivalent to 6.1 h at bankfull conditions, which seems reasonable given the flashy nature of floods in the Amargosa River.

River Migration over Decadal Time Scales

We conducted analysis on long-term precipitation and stream gage records to evaluate the

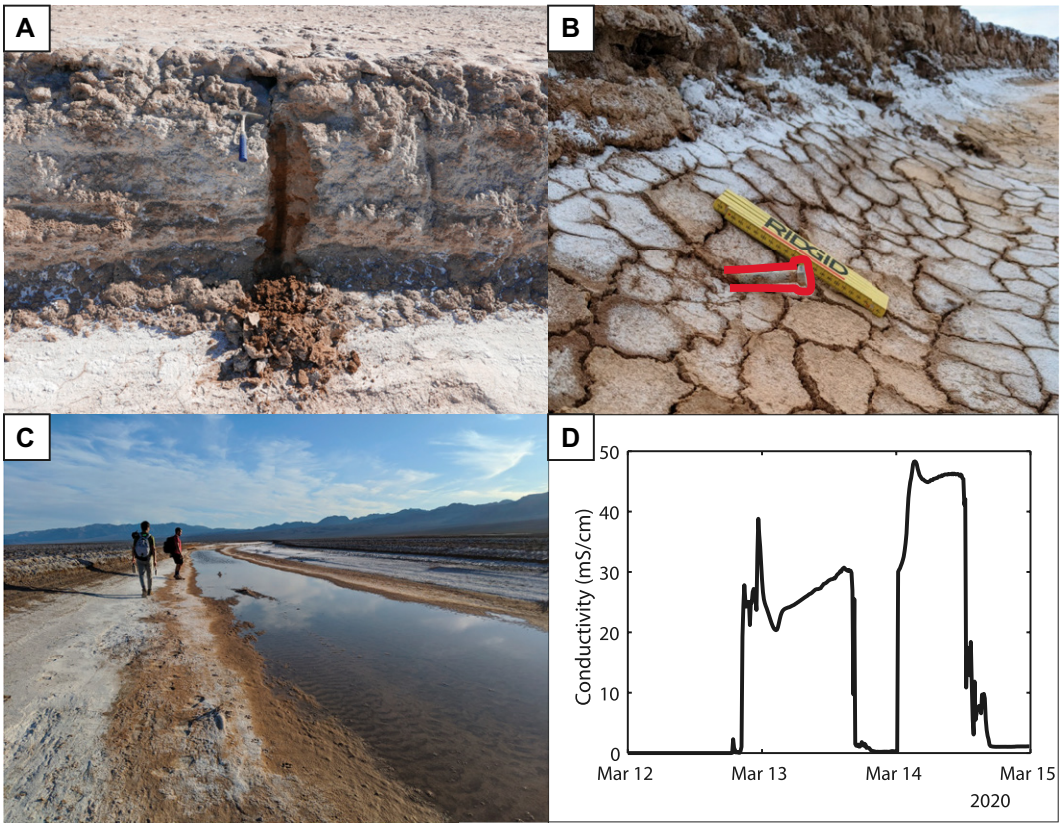

Figure 12. Amargosa River, Death Valley, California, USA. Salt crusts cover the channel bed and banks when the river is dry but dissolve completely when water flows through the channel. (A) Salt crusts on the river cutbank in Bend 1, with freshly exposed sediment appearing dark brown. (B) Erosion pin in Bend 1 exposed by flow event sticking out of apron of mud cracks. (C) Water ponded in the channels dissolved the surrounding salt crusts. Photo taken along the channel where Manning's *n* was measured (36.1137°N, 116.8267°W). (D) Water conductivity (mS/cm) varied throughout a single flow event.

frequency of erosive floods and compare the Amargosa to threshold channel theory. First, we scaled the peak water discharge observed at the USGS Tecopa gage to our field observations and predicted bank erosion rates along our study reach using our calibrated entrainment function (Equation 9). Then, we used the Amargosa's flood frequency distribution to evaluate the flood magnitude responsible for most geomorphic work from bank erosion.

To develop a scaling relation between peak water discharge at the Tecopa stream gage (Q_{Tecopa}; m^3/s) and our study site (Q_{DEVA}; m^3/s), we assumed that the magnitude of peak water discharge at each location follows linear relationship and fit the equation:

$$Q_{DEVA} = 0.0371 Q_{Tecopa} - 0.1180. \quad (10)$$

This linear relationship will be true if discharge follows a power-law relation with drainage area (Leopold et al., 1964), since the coefficient 0.0371 represents a ratio of drainage areas at each measuring site raised to a power. We fit this relationship using discharge records

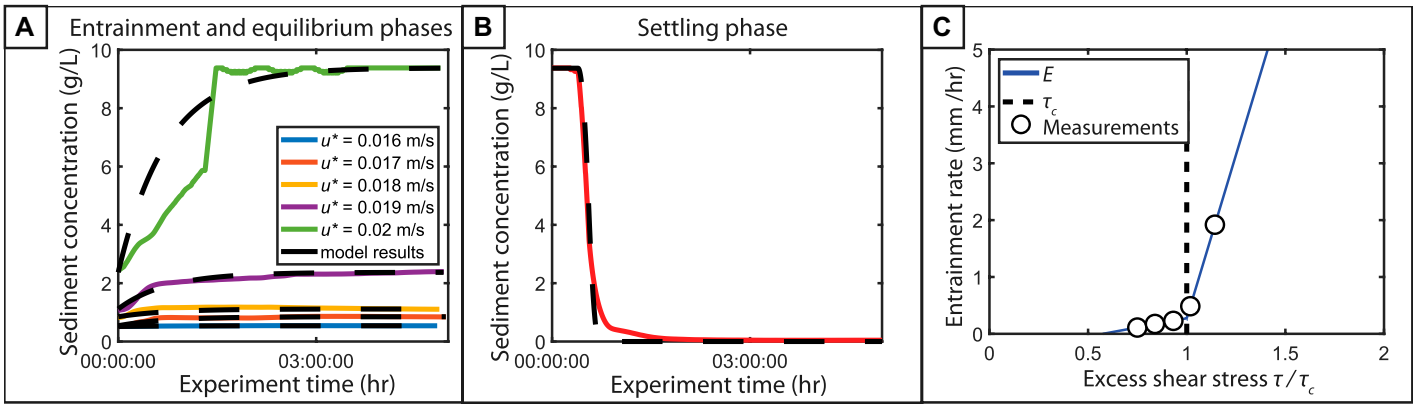

Figure 13. (A) Measured sediment concentration through time (hours) for each shear velocity (*u; m/s) during the entrainment and equilibrium phases, smoothed using a 2 min moving mean filter. Modeled sediment concentrations are shown as dashed black lines. (B) Sediment concentration through time (hours, measured in red and modeled in black dashed line) during the settling phase, smoothed using a 2 min moving mean filter. (C) Measured sediment entrainment rates as a function of shear stress (τ; Pa) divided by critical shear stress (τc; Pa) shown as white circles. We fit a piecewise function for entrainments rates as a function of fluid shear stress (Equation 9, blue solid line) and calculated the threshold of entrainment (black dotted line) as their intersection.**

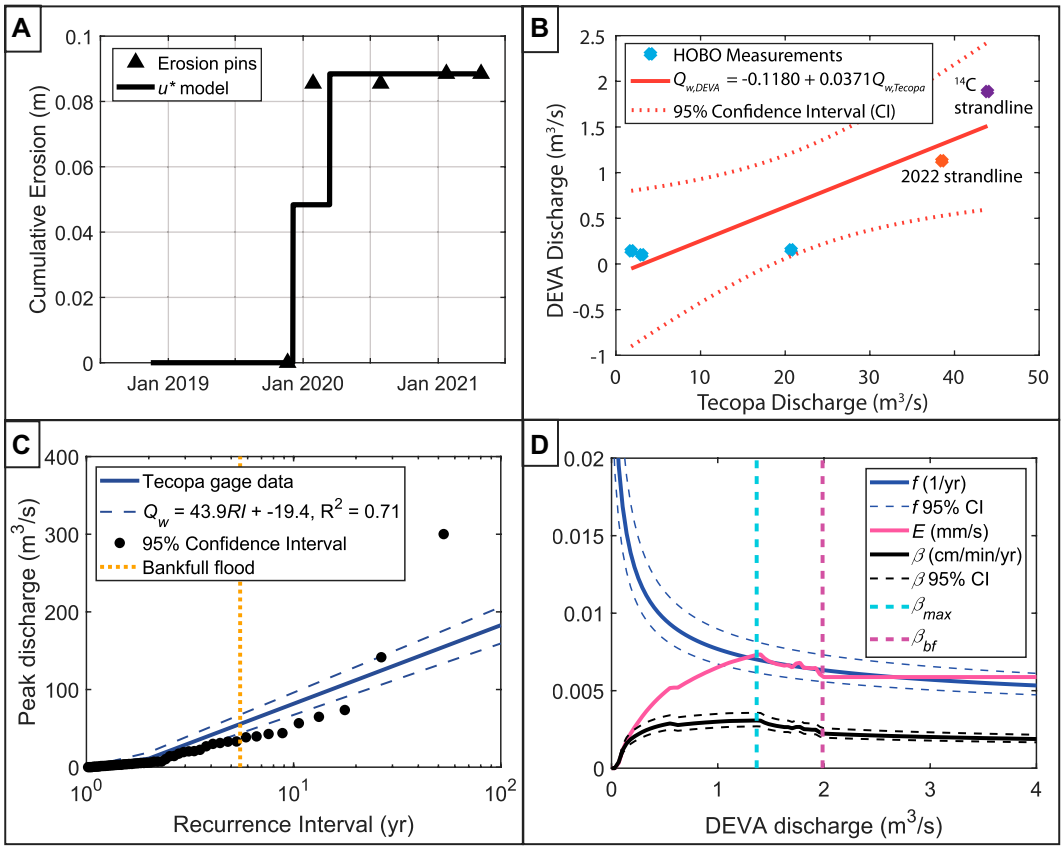

Figure 14. (A) Erosion pin measurements (black triangles) and cumulative bank erosion (black line) calculated using entrainment fluxes derived from mill experiments. (B) Combining our discharge measurements from the pressure sensor (blue diamonds) with ^{14}C dating of woody debris in a channel strandline (orange diamond) and the 2022 flood strandline (purple diamond), we found a linear relationship (red line; 95% confidence interval in dashed lines) between discharge at Tecopa, California, USA, and our monitoring site. (C) Comparison of our measurements with the long-term U.S. Geological Survey (USGS) stream gage record at Tecopa to evaluate the frequency and amount of bank erosion caused by different flood magnitudes. We fit a semi-logarithmic relation (blue line) between peak annual discharge and recurrence interval (*RI*) for the USGS gage (black circles) to calculate an event frequency model as 1/*RI*. The recurrence interval for a bankfull flood (5.5 years) is shown as a yellow dashed line. (D) We multiplied the flood frequency (*f*; blue dashed line) by the function for bank erosion calculated from excess shear stress (*E*; red dashed line) to calculate the bank erosion potential that occurs in Death Valley, California (β; solid black line). The discharge which accomplishes most bank erosion (β*max*) is shown as a dashed teal line and the bank erosion potential for a bankfull flood (β*bf*) is shown by the magenta dashed line. DEVA—our Death Valley study site; HOBO—data loggers used in study.

at Tecopa, discharges from the three smaller floods we observed, plus the ^{14}C dates from strandline woody debris. The radiocarbon dates matched well with a large flood that occurred in 2017, indicating the maximum flow depth for this event (Table 2), which we used to calculate discharge (Equations 2–4). Using these constraints, we calculated a ratio between the water discharge at Tecopa and our observation site (Fig. 14B). Although there is considerable uncertainty in this linear fit (see 95% confidence intervals on Fig. 14B), it indicates that the discharge at our study side is typically less than 10% of the discharge measured by the Tecopa gage.

To understand which flood magnitude played the most significant role in shaping the lower Amargosa River network, we calculated the bank erosion accomplished by a range of flood magnitudes. First, we used peak annual discharge at Tecopa to calculate recurrence interval of observed and bankfull floods (Fig. 14C). The frequency of each flood was calculated as the inverse of recurrence interval ($f = 1/RI$; 1/yr). We fit a logarithmic frequency distribution for flood frequencies, which tends to overestimate the magnitude of floods with $RI < 20$ yr and underestimate the magnitude of two recorded floods with $RI > 20$ yr.

To quantify bank erosion potential in a manner similar to geomorphic work (Wolman and Miller, 1960), we multiplied the event frequency distribution by the bank erosion rate at that discharge (E_{bank}; L/T). Assuming that bank erosion rates are equal to the experimental sediment entrainment rates ($E_{bank} = E_{expt}$; L/T), we calculate bank erosion potential (β; L/T^2) as

$$\beta = \frac{E_{bank}}{RI}. \quad (11)$$

Since the floodplain is very wide, we set all bank erosion potential for $H > H_{bf}$ equal to β_{bf}. We found that the highest bank erosion potential occurs at ~2/3 of bankfull discharge (Fig. 14D). Flood frequencies decrease exponentially, while the erosion rate gradually rises to a peak value of ~2.7 cm/hr at Q_{DEVA} ~1.3 m^3/s before gradually decreasing to a bankfull erosion rate of ~0.006 mm/s. The maximum in β occurs at the same discharge as the peak in erosion rate, and both E_{bank} and β peak at low discharges due to the channel geometry. The narrow inner channel focuses flow near the cutbank at low Q_{DEVA}, while water spreads out over the shallowly sloping point bar during high Q_{DEVA}, decreasing H_R and therefore τ_{bank}, u^*_{bank}, and E_{bank} despite the maximum flow depth continuing to increase.

Floodplain Stratigraphic Architecture

To quantify the relative importance of channel lateral migration versus avulsion for the lower Amargosa, we estimated the dimensionless channel mobility number (*M*) (Jerolmack and Mohrig, 2007):

$$M = \frac{\bar{h}v_c}{C_a B v_a}, \quad (12)$$

where $\bar{h}$ is the average channel depth (m), v_c is the channel lateral migration rate (m/yr), C_a is the number of active channels in the valley transect, B is the channel width (m), and v_a is the vertical aggradation rate (m/yr). When $M > 1$ the channel migrates rapidly across its floodplain relative to aggradation rates, forming amalgamated sandy channel bodies (e.g., Fig. 1D). For $M < 1$ the river migrates relatively slowly and forms narrow channel belts that aggrade to become superelevated, triggering avulsions and creating isolated sand bodies in mudstone. It has been argued that rivers changed from $M > 1$ to $M < 1$ with the proliferation of land plants (e.g., Valenza et al., 2023).

We calculated an upper bound for M along the Amargosa based on migration rates from Bends 1 and 2. We used $C_a = 6 \pm 4$ from the transect through Bend 1 (number of active channels along transect 8 with 1 standard deviation for the number of active channels per transect) and estimated long-term aggradation rates of $v_a = 7.7 \times 10^{-4}$ m/yr from the Badwater core (Lowenstein et al., 1999). We used the average migration rate measured over the 4-year study interval of $v_c = 0.05 \pm 0.02$ m/yr (mean ± 1SD) as well as the maximum migration rate of v_c ~1.5 m/yr reported by Ielpi (2019). These values should represent some of the highest channel lateral migration rates, since Bends 1 and 2 were some of the most sinuous bends on the floodplain and therefore should be migrating more rapidly than most other channels (Ielpi, 2019; Sylvester et al., 2019). Substituting these values of v_a and v_c with RTK GPS survey measurements of $H_R = 0.38 \pm 0.02$ m and $B = 6.86 \pm 0.02$ m into Equation 12 produced $M = 0.60 \pm 0.49$ using our v_c measurement and M ~18 using v_c from Ielpi (2019). This calculation suggests that only the highest sinuosity and most rapidly migrating channels of the Amargosa can keep up with valley aggradation rates, while most channels cannot. Therefore, the stratigraphy likely consists of amalgamated sandstones intermixed with isolated sandstone bodies in a muddy matrix.

A channel mobility number near one matches our observations of channel network morphology and previously published basin stratigraphy. There were a few visible cutoff bends on the floodplain intermixed with numerous abandoned channels and incipient avulsions that were growing by headward retreat of floodplains secondary channels (Fig. 6). River cutbanks contained structures, such as climbing ripple cross-strata, that indicated the Amargosa was eroding into fluvial deposits and not lacustrine deposits from Paleolake Manly (Fig. 8). High-resolution topography and field observations also did not reveal floodplain terraces, as would be expected if the Amargosa was incising into deposits from Lake Manly instead of constructing its own floodplain (Fig. 6). Sediment in cutbanks was generally finer-grained than in point bars, indicating that most cutbanks were eroding muddy floodplain deposits. Our observations agree with previous studies, where short cores taken in a transect across the floodplain by Hooke (1972) contained sandy deposits ~1–2 m thick embedded in mud, which is consistent with a stratigraphy of sandy channel bodies within predominantly muddy overbank material. The longer Badwater Basin core also supports this idea, as it shows a 7.7-m-thick accumulation of muddy floodplain deposits with a capping layer of primary halite (see "Study Site" section; Lowenstein et al., 1999). Together, these lines of evidence support that the Amargosa reworks its floodplain by both channel lateral migration and avulsion. This resulted in basin deposits characterized by isolated sandy channel-belt lenses within predominantly muddy overbank deposits.

DISCUSSION

The lower Amargosa River is a modern example of a meandering river with a muddy, self-formed, largely unvegetated floodplain. Vegetation cannot be a significant source of bank cohesion here since there are no plant roots in cutbanks (Fig. 8). Nonetheless, the Amargosa is meandering despite its lack of plants, with point bars keeping pace with cutbank erosion rates to maintain a narrow channel width. We observed point bars with lateral accretion surfaces that contained ripple cross-strata and had active ripples migrating across their surfaces (Fig. 8). Cutbank erosion occurred via collapse of subaerial slump blocks (on game camera timelapse; Fig. 10) and bank sediment entrainment (from erosion pins; Fig. 14B), as well as accretion of the channel bed and point bars during a bankfull flood event (Fig. 11). Lidar topography revealed that the Amargosa has maintained a narrow channel geometry over multiple flood events, allowing it to form cutoffs and abandoned channel loops (Fig. 6F). Therefore, our study reach of the Amargosa is actively meandering in the absence of vegetation.

Our field and experimental results supported that mud, and not salt, supplies the bank strength controlling the rate of lateral cutbank erosion. We found that water electrolytic conductivity changed throughout a single flood event, implying that the river water did not reach salt saturation during floods. In channels where we observed flowing water, all salt crusts were dissolved from the submerged channel bed and banks (Fig. 12C). We also observed pooled, stagnant water in Bend 1 that remained following a flood that had dissolved salt crusts on the bank and beds but left footprints and mud cracks intact. Therefore, a low flow event, which did not exceed the threshold of entrainment for bed sediment, managed to completely dissolve the salt crusts on the channel bed. Salt crusts might decrease the impact of small or short duration floods, which would not have time to dissolve all the salt and erode underlying mud, but we observed that salt crusts dissolved before the threshold for fluvial erosion was reached during longer floods. Importantly, our mud entrainment model, calibrated with experiments, accurately reproduced observed erosion pin rates showing that mud alone set the erodibility of the bank material.

While salt and vegetation did not limit cutbank erosion rates, they might play other roles to help retain mud in floodplain deposits. Salt crusts may help prevent mud from being eroded by wind, based on our observations that no sediment on the floodplain was mobilized by sustained 40 km/h winds except where salt crusts were broken or disrupted. In addition, trace organics may contribute to mud flocculation, increasing the settling velocity of sediment and promoting mud deposition across the floodplain (Zeichner et al., 2021; Nghiem et al., 2022). Flocculation can also be enhanced by high salinity (Mietta et al., 2009), and we observed flocs in our experiments and in reaches of the channel with water (see Movie S2). In addition, we inferred the presence of algae and microbial communities living on the floodplain from the production of foam on the flowing river visible in game camera timelapses, which may influence sediment transport (see Movie S3).

Threshold channel theory posits that the critical stress to erode the base of the riverbank sets the bankfull hydraulic geometry (Parker, 1978; Dunne and Jerolmack, 2020). We found that the Amargosa forms a channel cross-sectional geometry where bankfull flows far exceeded the threshold of erosion of the bank material. Bankfull flow occurred at 0.42 m average flow depth and 1.9 m^3/s water discharge, exerting ~1.6 times the critical shear stress to erode bank sediment. In contrast, the threshold to entrain bank sediment is surpassed for average flow depths of 0.26 m, so sub-bankfull flows can shape the river channel. Our measured critical shear stress, $\tau_c = 0.35$ Pa, falls on the lower range of values commonly reported for cohesive sediment of $0.1 \text{ Pa} < \tau_c < 5$ Pa (Winterwerp et al., 2012), and much lower than the 10 Pa required to fit a global data compilation of vegetated rivers (Dunne and Jerolmack, 2020). Thus, the Amargosa has much weaker banks than most vegetated rivers, but still is able to maintain stable meandering channels within a self-formed floodplain.

Our field measurements of bank erosion rates were slower than those of Ielpi (2019). We measured up to 7.1 cm of cutbank erosion from 2019 to 2023 using erosion pins on Bend 2, the bend shown in Figure 11B of Ielpi (2019). To address this discrepancy, we traced the top of cutbanks along Bend 2 by eye using the same images in Google Earth as Ielpi (2019) and used NAIP imagery from 2005 to 2020 in QGIS open-source software (see Fig. S1). Both methods reproduced results from Ielpi (2019), yielding erosion rates of 0.4–0.5 m/yr where we placed erosion pins and a maximum rate of ~1.5 m/yr upstream of the erosion pins. Most of the erosion occurred between 1995 and 2005, while erosion rates appear to have slowed from 2005 to 2020. This implies that cutbank erosion rates along the Amargosa vary significantly over decadal time scales, posing a challenge for measuring long-term channel migration rates. Specifically, most cutbanks erode <1 m/yr on average, so resolving bank erosion rates requires either short sequences of high-resolution imagery (such as NAIP) or long sequences of imagery with low or varying spatial resolution (the approach taken by Ielpi, 2019). Both approaches make it difficult to distinguish autogenic variability of river migration from changes in long-term migration rates, particularly since channel migration rates might vary throughout avulsion cycles. Unraveling the temporal variability in cutbank erosion rates is important because rapid migration of the Amargosa has been used to argue that unvegetated meandering rivers migrate more rapidly than vegetated meanders (e.g., Ielpi and Lapôtre, 2020).

Modern ephemeral rivers such as the Amargosa likely have migration rates set by the occurrence of large, infrequent storms, which complicates using these modern analogs to infer flood frequencies for channels on early Earth or Mars. While the Amargosa experiences flows that exceed the threshold of sediment transport with a similar frequency as perennial rivers (approximately every 2 years), these are generally low flows, and bankfull flows are rarer in this dryland river (5.5 years). The rarity of flow events is likely responsible for the highly intermittent channel migration, despite the Amargosa having much weaker banks than most vegetated rivers. For example, we recorded negligible cutbank erosion (<2 cm) over 3 years of observations and a maximum of 30.5 cm from the 2022 bankfull flood in our Bend 2, though sections of Bend 2 migrate at up to 1.5 m/yr over decadal time scales (Ielpi, 2019; Fig. 11B; Fig. S1). Our findings agree with the assessment of Wolman and Miller (1960), who found that dryland rivers have hydraulic geometries such that bankfull floods occur less frequently than rivers in wetter climates.

The Amargosa constructed its floodplain predominantly out of mud with isolated sandy channel belts implying that such a stratigraphic architecture can occur in the absence of vegetation. Our observations of mud cobbles, flocculation, and extensive networks of infilled channels that lack significant levees match those found in dryland rivers across the Great Basin (Hasson et al., 2023). Like many catchments in the Great Basin, Death Valley is a closed basin, which drives channel and floodplain aggradation and likely dictates a high fraction of mud in the Amargosa's deposits. In an open basin, cohesive sediment could instead be transported through the river to the coasts, decreasing bank cohesion and increasing migration rates while decreasing aggradation rates. In addition, the ephemeral Amargosa has a channel geometry adjusted to infrequent bankfull floods, while perennial streams appear to require a higher bank cohesion to maintain similar geometries (Dunne and Jerolmack, 2020). Therefore, while plants are not needed, an appropriate basin geometry, hydraulic regime, and sediment supply might be required to develop a stratigraphic architecture of channel-belt sandstones isolated within mud-rich floodplain deposits.

Vegetation-free dryland rivers have been used as potential analogs for Mars and early Earth (Matsubara et al., 2015). For the Amargosa, although muddy cutbanks are weaker than bank strengths inferred for vegetated rivers (Dunne and Jerolmack, 2020), mud slows cutbank erosion rates such that point bar aggradation can keep pace and the river can meander. Furthermore, the combination of muddy cutbanks and infrequent floods means that the Amargosa meanders slowly compared to long-term accretion rates, so avulsion rather than lateral migration is the dominant process that distributes sediment across Death Valley. Thus, mud alone (even in the absence of salt and vegetation) seems to be sufficient to permit river meandering (Lapôtre et al., 2019) and produce fluvial deposits with isolated sandstone bodies surrounded by mudstone. Although fluvial deposits of this type are typically thought to be characteristic of vegetated environments (Gibling and Davies, 2012), our results indicate early Earth and Mars could have hosted rivers with morphologies and deposit architectures similar to those present in modern terrestrial environments. In support of this argument, Mars has many examples of landforms called fluvial ridges, which likely formed by differential wind deflation of fluvial basin stratigraphy: mudstones are more easily eroded by the wind leaving sandy channel-belt deposits in positive relief (Matsubara et al., 2015; Dickson et al., 2021; Cardenas et al., 2022). Given the narrow widths of sinuous nature of many fluvial ridges, they most likely formed from strata that contained relatively narrow sandy channel belts within a basin otherwise dominated by mudstone (Hayden et al., 2019, 2021). Thus, these landforms and deposits on Mars appear similar to the Amargosa River in Death Valley.

CONCLUSIONS

We studied an unvegetated, sinuous reach of the Amargosa River on the floor of Death Valley to determine if it shared similar morphology and migration rates to vegetated meandering rivers. We found that the Amargosa was slowly meandering, with cutbank erosion pin measurements at two bends recording an average of 5.2 cm/yr from 2019 to 2023. The greatest cutbank erosion occurred during one bankfull flood, which caused an average of 18.5 cm of erosion, though rates of up to 1.5 m/yr were observed over two decades using satellite imagery. Sandy climbing ripples visible in both point bar and cutbank stratigraphy supported that the Amargosa was migrating through its own fluvial deposits, and not lacustrine deposits from Lake Manly. Besides its fine grain size and the prevalence of salt crusts, the Amargosa had a low slope and similar hydraulic geometry to meandering rivers in vegetated environments.

Lidar topography of the floodplain surfaces revealed many abandoned and infilled channels, including reaches that appear similar to oxbow lakes. Preferential flow routing during overbank floods formed channels via headward erosion, which we interpreted to record the initiation of frequent avulsions and subsequent channel abandonment by the Amargosa. The predominance of avulsion rather than migration as a mechanism to fill in Death Valley was supported by a moderate channel mobility number for the most rapidly migrating bends, which implied that a combination of avulsions and lateral migration resurfaced the floodplain. These processes were expected to produce basin stratigraphy consisting of isolated sandy bar deposits in muddy floodplain deposits, similar to those observed in previously published cores from Death Valley.

Threshold channel theory posits that a source of bank cohesion such as plant roots, mud, or salt is required to form deep, meandering channels and that the threshold flood required to erode the banks coincides with a bankfull flood. The Amargosa lacks plants on its cutbanks, and we determined that salt could not supply bank cohesion because we observed that it dissolved completely during flow events. To evaluate whether mud cohesion alone could account for bank erosion rates, we designed novel experiments to directly measure Amargosa bank sediment entrainment rates under different fluid shear

stress conditions. These experiments calibrated an entrainment relation that successfully replicated erosion pin data, indicating that mud provided bank cohesion sufficient for meandering in the absence of plants. Combining this entrainment relation with field measurements of flow depth and roughness, we were able to correlate flow and erosional events at our monitoring site to the USGS stream gage at Tecopa, California. Based on this decadal record, we found that erosional events were rare and significant bank erosion occurred at conditions below bankfull, in contrast to threshold channel theory.

ACKNOWLEDGMENTS

The authors thank Alex Beer, Austin Chadwick, Jan de Leeuw, Emily Geyman, Hemani Kalucha, Evelyn Lamb, Tien-Hao Liao, Freya Morris, Justin Ngheim, Zhongheng Sun, and Tom Ulizio for field assistance. We thank Sinéad Lyster, Alex Whittaker, and one anonymous reviewer for constructive comments that improved this manuscript. This work was conducted under National Park Service Permits DEVA-2018-SCI-0021, DEVA-2019-SCI-0025, and DEVA-2021-SCI-0003; and we would like to thank Ambre Chadouin, Richard Friese, Jane Lakeman, and Kevin Wilson for overseeing permitting and activities in Death Valley National Park. M.M. Douglas acknowledges support from the National Defense Science and Engineering Graduate Fellowship and the Resnick Sustainability Institute as well as the National Center for Airborne Laser Mapping (NCALM) Seed Proposal Program, which supported lidar collection.

REFERENCES CITED

Abernethy, B., and Rutherfurd, I.D., 2001, The distribution and strength of riparian tree roots in relation to riverbank reinforcement: Hydrological Processes, v. 15, p. 63–79, https://doi.org/10.1002/hyp.152.

Baldridge, A.M., Farmer, J.D., and Moersch, J.E., 2004, Mars remote-sensing analog studies in the Badwater Basin, Death Valley, California: Journal of Geophysical Research: Planets, v. 109, E12006, https://doi.org/10.1029/2004JE002315.

Burr, D.M., Enga, M.-T., Williams, R.M.E., Zimbelman, J.R., Howard, A.D., and Brennand, T.A., 2009, Pervasive aqueous paleoflow features in the Aeolis/Zephyria Plana region, Mars: Icarus, v. 200, p. 52–76, https://doi.org/10.1016/j.icarus.2008.10.014.

Cardenas, B.T., Lamb, M.P., and Grotzinger, J.P., 2022, Martian landscapes of fluvial ridges carved from ancient sedimentary basin fill: Nature Geoscience, v. 15, p. 871–877, https://doi.org/10.1038/s41561-022-01058-2.

Corenblit, D., and Steiger, J., 2009, Vegetation as a major conductor of geomorphic changes on the Earth surface: Toward evolutionary geomorphology: Earth Surface Processes and Landforms, v. 34, p. 891–896, https://doi.org/10.1002/esp.1788.

DiBiase, R.A., Limaye, A.B., Scheingross, J.S., Fischer, W.W., and Lamb, M.P., 2013, Deltaic deposits at Aeolis Dorsa: Sedimentary evidence for a standing body of water on the northern plains of Mars: Journal of Geophysical Research: Planets, v. 118, p. 1285–1302, https://doi.org/10.1002/jgre.20100.

Dickson, J.L., Lamb, M.P., Williams, R.M.E., Hayden, A.T., and Fischer, W.W., 2021, The global distribution of depositional rivers on early Mars: Geology, v. 49, p. 504–509, https://doi.org/10.1130/G48457.1.

Dietrich, W.E., 1982, Settling velocity of natural particles: Water Resources Research, v. 18, p. 1615–1626, https://doi.org/10.1029/WR018i006p01615.

Dong, T.Y., Nittrouer, J.A., Czapiga, M.J., Ma, H., McElroy, B., Il'icheva, E., Pavlov, M., Chalov, S., and Parker, G., 2019, Roles of bank material in setting bankfull hydraulic geometry as informed by the Selenga River Delta, Russia: Water Resources Research, v. 55, p. 827–846, https://doi.org/10.1029/2017WR021985.

Douglas, M.M., Li, G.K., Fischer, W.W., Rowland, J.C., Kemeny, P.C., West, A.J., Schwenk, J., Piliouras, A.P., Chadwick, A.J., and Lamb, M.P., 2022, Organic carbon burial by river meandering partially offsets bank erosion carbon fluxes in a discontinuous permafrost floodplain: Earth Surface Dynamics, v. 10, p. 421–435, https://doi.org/10.5194/esurf-10-421-2022.

Dunne, K.B.J., and Jerolmack, D.J., 2020, What sets river width?: Science Advances, v. 6, https://doi.org/10.1126/sciadv.abc1505.

Eke, E., Parker, G., and Shimizu, Y., 2014, Numerical modeling of erosional and depositional bank processes in migrating river bends with self-formed width: Morphodynamics of bar push and bank pull: Journal of Geophysical Research: Earth Surface, v. 119, p. 1455–1483, https://doi.org/10.1002/2013JF003020.

Ganti, V., Whittaker, A.C., Lamb, M.P., and Fischer, W.W., 2019, Low-gradient, single-threaded rivers prior to greening of the continents: Proceedings of the National Academy of Sciences of the United States of America, v. 116, p. 11,652–11,657, https://doi.org/10.1073/pnas.1901642116.

Garcia, M., and Parker, G., 1991, Entrainment of bed sediment into suspension: Journal of Hydraulic Engineering, v. 117, p. 414–435, https://doi.org/10.1061/(ASCE)0733-9429(1991)117:4(414).

Gee, G.W., and Or, D., 2002, Particle-size analysis, *in* Dane, J.H., and Topp, G.C., eds., Methods of Soil Analysis Part 4: Physical Methods: Madison, Wisconsin, Soil Science Society of America, Inc., Soil Science Society of America Book Series 5, p. 255–293.

Gibling, M.R., and Davies, N.S., 2012, Palaeozoic landscapes shaped by plant evolution: Nature Geoscience, v. 5, p. 99–105, https://doi.org/10.1038/ngeo1376.

Hanson, G.J., and Simon, A., 2001, Erodibility of cohesive streambeds in the loess area of the midwestern USA: Hydrological Processes, v. 15, p. 23–38, https://doi.org/10.1002/hyp.149.

Hartley, A.J., Owen, A., Swan, A., Weissmann, G.S., Holzweber, B.I., Howell, J., Nichols, G., and Scuderi, L., 2015, Recognition and importance of amalgamated sandy meander belts in the continental rock record: Geology, v. 43, p. 679–682, https://doi.org/10.1130/G36743.1.

Hasson, M., Marvin, M.C., Gunn, A., Ielpi, A., and Lapôtre, M.G.A., 2023, A depositional model for meandering rivers without land plants: Sedimentology, v. 70, no. 7, p. 2272–2301, https://doi.org/10.1111/sed.13121.

Hayden, A.T., Lamb, M.P., Fischer, W.W., Ewing, R.C., McElroy, B.J., and Williams, R.M.E., 2019, Formation of sinuous ridges by inversion of river-channel belts in Utah, USA, with implications for Mars: Icarus, v. 332, p. 92–110, https://doi.org/10.1016/j.icarus.2019.04.019.

Hayden, A.T., Lamb, M.P., and Carney, A.J., 2021, Similar curvature-to-width ratios for channels and channel belts: Implications for paleo-hydraulics of fluvial ridges on Mars: Geology, v. 49, p. 837–841, https://doi.org/10.1130/G48370.1.

Hooke, R.L., 1972, Geomorphic evidence for late-Wisconsin and Holocene tectonic deformation, Death Valley, California: Geological Society of America Bulletin, v. 83, p. 2073–2098, https://doi.org/10.1130/0016-7606(1972)83[2073:GEFLAH]2.0.CO;2.

Hua, Q., Turnbull, J.C., Santos, G.M., Rakowski, A.Z., Ancapichún, S., De Pol-Holz, R., Hammer, S., Lehman, S.J., Levin, I., Miller, J.B., Palmer, J.G., and Turney, C.S.M., 2022, Atmospheric radiocarbon for the period 1950–2019: Radiocarbon, v. 64, p. 723–745, https://doi.org/10.1017/RDC.2021.95.

Ielpi, A., 2019, Morphodynamics of meandering streams devoid of plant life: Amargosa River, Death Valley, California: Geological Society of America Bulletin, v. 131, p. 782–802, https://doi.org/10.1130/B31960.1.

Ielpi, A., and Lapôtre, M.G.A., 2019, Barren meandering streams in the modern Toiyabe Basin of Nevada, U.S.A., and their relevance to the study of the pre-vegetation rock record: Journal of Sedimentary Research, v. 89, p. 399–415, https://doi.org/10.2110/jsr.2019.25.

Ielpi, A., and Lapôtre, M.G.A., 2020, A tenfold slowdown in river meander migration driven by plant life: Nature Geoscience, v. 13, p. 82–86, https://doi.org/10.1038/s41561-019-0491-7.

Ielpi, A., and Rainbird, R.H., 2015, Architecture and morphodynamics of a 1·6 Ga fluvial sandstone: Ellice Formation of Elu Basin, Arctic Canada: Sedimentology, v. 62, p. 1950–1977, https://doi.org/10.1111/sed.12211.

Ielpi, A., Lapôtre, M.G.A., Gibling, M.R., and Boyce, C.K., 2022, The impact of vegetation on meandering rivers: Nature Reviews Earth & Environment, v. 3, p. 165–178, https://doi.org/10.1038/s43017-021-00249-6.

Jerolmack, D.J., and Mohrig, D., 2007, Conditions for branching in depositional rivers: Geology, v. 35, p. 463–466, https://doi.org/10.1130/G23308A.1.

Julian, J.P., and Torres, R., 2006, Hydraulic erosion of cohesive riverbanks: Geomorphology, v. 76, p. 193–206, https://doi.org/10.1016/j.geomorph.2005.11.003.

Kim, W., Connell, S.D., Steel, E., Smith, G.A., and Paola, C., 2011, Mass-balance control on the interaction of axial and transverse channel systems: Geology, v. 39, p. 611–614, https://doi.org/10.1130/G31896.1.

Kleinhans, M.G., de Vries, B., Braat, L., and van Oorschot, M., 2018, Living landscapes: Muddy and vegetated floodplain effects on fluvial pattern in an incised river: Earth Surface Processes and Landforms, v. 43, p. 2948–2963, https://doi.org/10.1002/esp.4437.

Kopp, J., and Kim, W., 2015, The effect of lateral tectonic tilting on fluviodeltaic surficial and stratal asymmetries: Experiment and theory: Basin Research, v. 27, p. 517–530, https://doi.org/10.1111/bre.12086.

Ku, T.-L., Luo, S., Lowenstein, T.K., Li, J., and Spencer, R.J., 1998, U-Series chronology of lacustrine deposits in Death Valley, California: Quaternary Research, v. 50, p. 261–275, https://doi.org/10.1006/qres.1998.1995.

Langhorst, T., and Pavelsky, T., 2023, Global observations of riverbank erosion and accretion from Landsat imagery: Journal of Geophysical Research: Earth Surface, v. 128, https://doi.org/10.1029/2022JF006774.

Lapôtre, M.G.A., Ielpi, A., Lamb, M.P., Williams, R.M.E., and Knoll, A.H., 2019, Model for the formation of single-thread rivers in barren landscapes and implications for pre-Silurian and Martian fluvial deposits: Journal of Geophysical Research: Earth Surface, v. 124, p. 2757–2777, https://doi.org/10.1029/2019JF005156.

Leopold, L.B., and Wolman, M.G., 1957, River channel patterns: Braided, meandering, and straight: U.S. Geological Survey Numbered Series 282-B, 50 p., https://doi.org/10.3133/pp282B.

Leopold, L.B., Wolman, M.G., and Miller, J.P., 1964, Fluvial Processes in Geomorphology: New York, Dover Publications, 544 p.

Li, J., Lowenstein, T.K., Brown, C.B., Ku, T.-L., and Luo, S., 1996, A 100 ka record of water tables and paleoclimates from salt cores, Death Valley, California: Palaeogeography, Palaeoclimatology, Palaeoecology, v. 123, p. 179–203, https://doi.org/10.1016/0031-0182(95)00123-9.

Li, J., Bristow, C.S., Luthi, S.M., and Donselaar, M.E., 2015, Dryland anabranching river morphodynamics: Río Capilla, Salar de Uyuni, Bolivia: Geomorphology, v. 250, p. 282–297 https://doi.org/10.1016/j.geomorph.2015.09.011.

Long, D.G.F., 1978, Depositional environments of a thick Proterozoic sandstone: The (Huronian) Mississagi Formation of Ontario, Canada: Canadian Journal of Earth Sciences, v. 15, p. 190–206, https://doi.org/10.1139/e78-020.

Lowenstein, T.K., Li, J., Brown, C., Roberts, S.M., Ku, T.-L., Luo, S., and Yang, W., 1999, 200 k.y. paleoclimate record from Death Valley salt core: Geology, v. 27, p. 3–6, https://doi.org/10.1130/0091-7613(1999)027<0003:KYPRFD>2.3.CO;2.

Malin, M.C., and Edgett, K.S., 2003, Evidence for persistent flow and aqueous sedimentation on early Mars: Science, v. 302, p. 1931–1934, https://doi.org/10.1126/science.1090544.

Matsubara, Y., Howard, A.D., Burr, D.M., Williams, R.M.E., Dietrich, W.E., and Moore, J.M., 2015, River meandering on Earth and Mars: A comparative study of Aeolis

Dorsa meanders, Mars and possible terrestrial analogs of the Usuktuk River, AK, and the Quinn River, NV: Geomorphology, v. 240, p. 102–120, https://doi.org/10.1016/j.geomorph.2014.08.031.

McMahon, W.J., and Davies, N.S., 2018, The shortage of geological evidence for pre-vegetation meandering rivers, *in* Ghinassi, M., Colombera, L., Mountney, N.P., Reesink, A.J.H., and Bateman, M., eds., Fluvial Meanders and Their Sedimentary Products in the Rock Record: John Wiley & Sons, p. 119–148, https://doi.org/10.1002/9781119424437.ch5.

Métivier, F., Lajeunesse, E., and Devauchelle, O., 2017, Laboratory rivers: Lacey's law, threshold theory, and channel stability: Earth Surface Dynamics, v. 5, p. 187–198, https://doi.org/10.5194/esurf-5-187-2017.

Mietta, F., Chassagne, C., Manning, A.J., and Winterwerp, J.C., 2009, Influence of shear rate, organic matter content, pH and salinity on mud flocculation: Ocean Dynamics, v. 59, p. 751–763, https://doi.org/10.1007/s10236-009-0231-4.

Millar, R.G., 2000, Influence of bank vegetation on alluvial channel patterns: Water Resources Research, v. 36, p. 1109–1118, https://doi.org/10.1029/1999WR900346.

Millar, R.G., 2005, Theoretical regime equations for mobile gravel-bed rivers with stable banks: Geomorphology, v. 64, p. 207–220, https://doi.org/10.1016/j.geomorph.2004.07.001.

Millar, R.G., and Quick, M.C., 1998, Stable width and depth of gravel-bed rivers with cohesive banks: Journal of Hydraulic Engineering, v. 124, p. 1005–1013, https://doi.org/10.1061/(ASCE)0733-9429(1998)124:10(1005).

Nghiem, J.A., Fischer, W.W., Li, G.K., and Lamb, M.P., 2022, A mechanistic model for mud flocculation in freshwater rivers: Journal of Geophysical Research: Earth Surface, v. 127, https://doi.org/10.1029/2021JF006392.

OpenTopography, 2020, Meandering Channels in Death Valley, CA 2019: https://doi.org/10.5069/G96D5R55.

Parker, G., 1976, On the cause and characteristic scales of meandering and braiding in rivers: Journal of Fluid Mechanics, v. 76, p. 457–480, https://doi.org/10.1017/S0022112076000748.

Parker, G., 1978, Self-formed straight rivers with equilibrium banks and mobile bed. Part 2. The gravel river: Journal of Fluid Mechanics, v. 89, p. 127–146, https://doi.org/10.1017/S0022112078002505.

Parker, G., Shimizu, Y., Wilkerson, G.V., Eke, E.C., Abad, J.D., Lauer, J.W., Paola, C., Dietrich, W.E., and Voller, V.R., 2011, A new framework for modeling the migration of meandering rivers: Earth Surface Processes and Landforms, v. 36, p. 70–86, https://doi.org/10.1002/esp.2113.

Partheniades, E., 1965, Erosion and deposition of cohesive soils: Journal of the Hydraulics Division, v. 91, p. 105–139, https://doi.org/10.1061/JYCEAJ.0001165.

Phillips, C.B., and Jerolmack, D.J., 2016, Self-organization of river channels as a critical filter on climate signals: Science, v. 352, p. 694–697, https://doi.org/10.1126/science.aad3348.

Pollen-Bankhead, N., and Simon, A., 2009, Enhanced application of root-reinforcement algorithms for bank-stability modeling: Earth Surface Processes and Landforms, v. 34, p. 471–480, https://doi.org/10.1002/esp.1690.

Reimer, P.J., et al., 2013, IntCal13 and Marine13 radiocarbon age calibration curves 0–50,000 years cal BP: Radiocarbon, v. 55, p. 1869–1887, https://doi.org/10.2458/azu_js_rc.55.16947.

Reimer, R.W., and Reimer, P.J., 2023, CALIBomb: https://calib.org/CALIBomb/ (accessed June 2021).

Ritter, B., Diederich-Leicher, J.L., Binnie, S.A., Stuart, F.M., Wennrich, V., Bolten, A., and Dunai, T.J., 2022, Impact of $CaSO_4$-rich soil on Miocene surface preservation and Quaternary sinuous to meandering channel forms in the hyperarid Atacama Desert: Scientific Reports, v. 12, 17951, https://doi.org/10.1038/s41598-022-22787-9.

Rouse, H., 1937, Modern conceptions of the mechanics of fluid turbulence: Transactions of the American Society of Civil Engineers, v. 102, p. 463–505, https://doi.org/10.1061/TACEAT.0004872.

Santos, M.G.M., and Owen, G., 2016, Heterolithic meandering-channel deposits from the Neoproterozoic of NW Scotland: Implications for palaeogeographic reconstructions of Precambrian sedimentary environments: Precambrian Research, v. 272, p. 226–243, https://doi.org/10.1016/j.precamres.2015.11.003.

Santos, M.G.M., Hartley, A.J., Mountney, N.P., Peakall, J., Owen, A., Merino, E.R., and Assine, M.L., 2019, Meandering rivers in modern desert basins: Implications for channel planform controls and prevegetation rivers: Sedimentary Geology, v. 385, p. 1–14, https://doi.org/10.1016/j.sedgeo.2019.03.011.

Scheingross, J.S., Brun, F., Lo, D.Y., Omerdin, K., and Lamb, M.P., 2014, Experimental evidence for fluvial bedrock incision by suspended and bedload sediment: Geology, v. 42, p. 523–526, https://doi.org/10.1130/G35432.1.

Sklar, L.S., and Dietrich, W.E., 2001, Sediment and rock strength controls on river incision into bedrock: Geology, v. 29, p. 1087–1090, https://doi.org/10.1130/0091-7613(2001)029<1087:SARSCO>2.0.CO;2.

Sweeney, M.R., Fischer, B., Wermers, K., and Cowman, T., 2019, Eolian and fluvial modification of Missouri River sandbars deposited by the 2011 flood, USA: Geomorphology, v. 327, p. 111–125, https://doi.org/10.1016/j.geomorph.2018.10.018.

Sweet, I.P., 1988, Early Proterozoic stream deposits: Braided or meandering—Evidence from central Australia: Sedimentary Geology, v. 58, p. 277–293, https://doi.org/10.1016/0037-0738(88)90073-5.

Sylvester, Z., Durkin, P., and Covault, J.A., 2019, High curvatures drive river meandering: Geology, v. 47, p. 263–266, https://doi.org/10.1130/G45608.1.

Trower, E.J., Lamb, M.P., and Fischer, W.W., 2017, Experimental evidence that ooid size reflects a dynamic equilibrium between rapid precipitation and abrasion rates: Earth and Planetary Science Letters, v. 468, p. 112–118, https://doi.org/10.1016/j.epsl.2017.04.004.

Valenza, J.M., Ganti, V., Whittaker, A.C., and Lamb, M.P., 2023, Pre-vegetation, single-thread rivers sustained by cohesive, fine-grained bank sediments: Mesoproterozoic Stoer Group, NW Scotland: Geophysical Research Letters, v. 50, https://doi.org/10.1029/2023GL104379.

Vanoni, V.A., and Brooks, N.H., 1957, Laboratory studies of the roughness and suspended load of alluvial streams: California Institute of Technology M.R.D. Sediment Series Report or Paper 11, 130 p., https://resolver.caltech.edu/CaltechKHR:SedLabRpt-E-68 (accessed December 2022).

Winterwerp, J.C., van Kesteren, W.G.M., van Prooijen, B., and Jacobs, W., 2012, A conceptual framework for shear flow–induced erosion of soft cohesive sediment beds: Journal of Geophysical Research: Oceans, v. 117, https://doi.org/10.1029/2012JC008072.

Wolman, M.G., and Miller, J.P., 1960, Magnitude and frequency of forces in geomorphic processes: The Journal of Geology, v. 68, p. 54–74, https://doi.org/10.1086/626637.

Zeichner, S.S., Nghiem, J., Lamb, M.P., Takashima, N., de Leeuw, J., Ganti, V., and Fischer, W.W., 2021, Early plant organics increased global terrestrial mud deposition through enhanced flocculation: Science, v. 371, p. 526–529, https://doi.org/10.1126/science.abd0379.

Science Editor: Brad Singer
Associate Editor: Emmanuel Gabet

Manuscript Received 5 September 2023
Revised Manuscript Received 6 June 2024
Manuscript Accepted 24 June 2024